Lα INTENSITY IN CORONAL STREAMERS

G. NOCI
Dipartimento di Astronomia e Scienza dello Spazio, Università di Firenze, Italy

G. POLETTO
Osservatorio Astrofisico di Arcetri, Largo Enrico Fermi, 5, 50125 Firenze, Italy

S. T. SUESS
NASA Marshall Space Flight Center, SSL/ES52, Huntsville, AL 35812, U.S.A.

and

A.-H. WANG and S. T. WU
Center for Space Plasma and Aeronomic Research, The University of Alabama in Huntsville, Huntsville, AL 35899, U.S.A.

(Received 21 August, 1992; in revised form 5 February, 1993)

Abstract. White-light images are presently the primary source of information on physical conditions in the solar corona at distances greater than a few tenths of a solar radius above the limb. As a consequence, we still only have an incomplete description of structures extending beyond the solar limb. In particular, streamers, although observed for decades, represent a poorly known phenomenon. SOHO, to be launched in 1995, will be able to make long-term observations of these features up to heights of a few $R_\odot$, both in white light and UV. In this paper we present simulations of Lα intensity in coronal streamers, based on the two-dimensional (2-D) model developed by Wang *et al.* (1992, 1993) via a time-dependent numerical relaxation approach. Because the model is 2-D, we make an *a priori* hypothesis about the extension of streamers in the third dimension. Lα data, obtained from a rocket (Kohl *et al.*, 1983), allowed us to identify a shape which fits the observations. We consider streamers with different magnetic field configurations and at different position angles with respect to the plane of the sky to illustrate how different regions along the line of sight contribute to the emergent intensity. Our purpose is twofold: to provide guidelines for UVCS observational operations and to explore the parameter space in order to understand the role of geometric factors and of the physical state of the corona in determining the overall streamer brightness. We conclude by showing how the results guide the future development of streamer models.

1. Introduction

Before the advent of coronagraphs, eclipses offered the only means to observe the solar corona. In spite of the short time over which coronal structures were visible, their basic characteristics have been reproduced in beautiful drawings (see, e.g., Foukal, 1990), which prove that streamers – the most prominent white-light coronal features – had been known and observed for decades. Following earlier balloon-borne coronagraph experiments (Newkirk and Bohlin, 1965; Dollfus, Fort, and Morel, 1968), different techniques have become available, and radio telescopes (see, e.g., Gopalswamy, Kundu, and Szabo, 1987) and space experiments (see, e.g., for Skylab, Hildner *et al.*, 1975; Poland, 1978; for SMM, Illing and Hundhausen, 1986; Kahler, 1991) collected a wealth of data on these large-scale features, which, nevertheless, remain poorly known. We know that streamers, at the time of solar activity minimum, are concentrated along the solar equator in a belt, which broadens

Solar Physics **147:** 73–96, 1993.

NASA
National Aeronautical and Space Agency

Report Document Page

1. Report No.	2. Government Accession No.	3. Recipient's Catalog No.
Final		

4. Title and Subtitle
Model Development for Ulysses and SOHO

5. Report Due
10/27/93

6. Performing Organization Code
University of Alabama in Huntsville

7. Aurthor(s)
S. T. Wu

8. Performing Organization Report No.
Final

10. Work Unit No.

9. Performing Organization Name and Address
University of Alabama in Huntsville
Huntsville, Alabama 35899

11. Contract or Grant No.
NAS8-38609 DO 68

12. Sponsoring Agency Name and Address
National Aeronautics and Space Administration
Washington, D.C. 20546-001
Marshall Space Flight Center, AL 35812

13. Type of report and Period covered
5/27/93 - 11/27/93
Draft Final

14. Sponsoring Agency Code

15. Supplementary Notes

16.Abstract

Provide scientific expertise in solar physics and in the development and use of magnetohydrodynamic (MHD) models of coronal stuctures for the computation of Lyman alpha scattered radiation in these structures. The specific objectives will be to run MHD models with new boundary conditions and compute resulting scattered solar Lyman alpha intensities, guided by results from the first series of boundary conditions.

17. Key Words (Suggested by Author(s))
SOHO, Ulysses, MHD, Lyman, corona

18. Distribution Statement
CN22D(3). AT01 (1), EM13/L.Smith (1)
ONRRR (1), Suess/ES52 (1+repro)
NASA Sci & Tech Info. Fac. (1+repro)
Vaughn/UAH (1)

19. Security Class. (of this report)	20. Security Class. (of this page)	21. No. of pages	22. Price
Unclassified	Unclassified		

NASA FORM 1626 OCT 86

During past several months we have established a two-dimensinal time-dependent numerical MHD model to do the numerical simulation of large scale coronal structure with coronal streamers and coronal holes. The motivation for this study is to develop a tool for the interpretation of the observations to be obtained from UVCS and LASCO experiments on board the upcoming SOHO mission.

First, we have simulated coronal streamers and given four examples. Please see attached papers for the details.

Then we simulated the streamers and holes simultaneously. In this study the initial density and temperature given are not homogeneous from the pole to the equator. The density decreases from the equator to the pole. The temperature increases from the equator to the pole to get high velocity at the pole, since we used the polytropic state equation instead of the real energy equation and this temperature is effective temperature. According to density and temperature distribution the initial Parker's solution has been obtained along each altitude direction from the pole to the equator. In the steady state at the hole region the high solar wind with low density has be achieved, and at the streamer region the low solar wind with high density, especily at the closed field region with almost zero velocity and high density, has been achieved simultaneously. The results are entitled "Simulation of Streamers with Coronal Holes" by S. T. Suess, S. T. Wu, A. H. Wang and G. Poletto were presented at the Second SOHO Workshop at Elba, Italy and will be published in the proceedings (in press) Kluwer Publishers, 1994.

to cover a wider range of latitudes, at other epochs. We know that streamers are stable structures, which may last for several rotations (see, e.g., Poland, 1978). However, we know little about the formation, or the disruption, of streamers: we have only a few observations, for instance, of the contraction of a post/mass ejection structure to form a streamer (see, e.g., Illing and Hundhausen, 1986). As to the physical properties of streamers, our knowledge is limited, as we will discuss later on, to an incomplete understanding of their density structure. This situation may in part be ascribed to the fact that spectroscopic instruments were unable to operate at the large heights reached by streamers, which therefore have been observed mainly in white light. On the other hand, the solar community seemed to have little interest in streamers: no review article has been dedicated to these structures for years, notwithstanding the steady proliferation of scientific papers.

However, streamers are relevant to a number of problems. They represent the ideal structures to investigate the differences in temperature, density, flow velocities, and magnetic field structure between magnetically closed and open areas and to gain some insight into the physical conditions of current sheet regions, which purportedly occur in streamers. Koutchmy (1988) pointing out how tangential discontinuities are almost systematically parts of large streamers, noticed how their analysis would offer the best estimate of the magnetic field value in the corona, provided that the temperature keeps constant across the discontinuity. The capabilities of streamers in providing data crucial to the solution of these questions have hardly been exploited.

In solar wind physics streamers play an ambiguous role. It has been claimed (see, e.g., Feldman *et al.*, 1981) that they constitute the major source of the interstream and low speed solar wind, but we know neither how large is the contribution of streamers to the solar wind mass flux, nor the geometry of the open field lines associated with streamers, along which the wind purportedly propagates. The reason for the depletion of helium, which seems to accompany the slow wind from streamers (see, e.g., Gosling *et al.*, 1981), is not well understood.

In the future, SOHO instrumentation will offer us a means to learn more about these structures. In particular, UVCS will be able to make EUV observations of streamers, up to $\leq 10\ R_\odot$, over an extended period of time, thus allowing us to get a new kind of data whose capabilities have not yet been explored. In order to provide guidelines to be used in devising UVCS observational sequences, we present, in this paper, a variety of simulated, typical Lα observations of streamers. As a basis for our simulations, we adopt the two-dimensional streamer model, developed by Wang *et al.* (1992, 1993), which is summarized in Section 2. After comparing, in Section 3, the model predictions with observations of densities in streamers, we calculate, in Section 4, the Lα emission from different streamer configurations and, in Section 5, we simulate Lα observations of a streamer carried around by solar rotation. Finally, in the Discussion, we illustrate some future development of our work.

2. The Streamer Model

The physical streamer models that we use for calculating Lα intensities are the result of a numerical simulation of global coronal structure. The simulation is a solution of the magnetohydrodynamic equations for two-dimensional, axisymmetric, single fluid, polytropic, time-dependent flow. The steady state is found by starting with an essentially arbitrary initial state having the desired boundary conditions and allowing a relaxation in time until the solution is no longer changing. The resulting model is therefore assured both of being a self-consistent solution for the specified physical boundary conditons and of being stable. The model, since axisymmetric, describes a single continuous streamer that extends all the way around the Sun at a specific latitude. The simulation is further described by Wang *et al.* (1992, 1993).

The boundary conditions at 1 $R_\odot$ are that the temperature and density are constant in latitude and that the vector magnetic field is a potential magnetic field. Three magnetic field geometries are used: a dipole, a quadrupole, and a hexapole; the scalar potentials are proportional to $P_2(\cos\theta)$, $P_3(\cos\theta)$, and $P_4(\cos\theta)$, respectively. There are two dimensionless numbers: the polytropic index, γ, and the ratio of internal to magnetic energy densities, β. We use $\gamma = 1.05$ in all cases, $\beta = 1.0$ for all three field geometries, and, in addition, do a dipole calculation for $\beta = 0.2$. In these cases, β is evaluated at 1.0 $R_\odot$ at the equator, where the field strength is 1.67 G for both $\beta = 1.0$ and $\beta = 0.2$. For the high β case, the base temperature and density are 1.8×10^6 K and 2.25×10^8 cm^{-3}. For the low β case, they are 1.44×10^6 K and 5.61×10^7 cm^{-3}. The three magnetic field geometries naturally lead to a single equatorial streamer, a mid-latitude streamer, and both an equatorial and a mid-latitude streamer for the dipole, quadrupole, and hexapole, respectively.

The simulation extends from 1.0 $R_\odot$ to 15.0 $R_\odot$ and from pole to equator. The boundary conditions are symmetric about the equator, so a solution in the opposite hemisphere is not necessary. In this paper, we only quote results inside 7.0 $R_\odot$ because this covers the range over which closed streamer structures most frequently are observed. There are 20 grid points between the pole and equator, 27 gridpoints between 1.0 $R_\odot$ and 7.0 $R_\odot$. The initial state consists of a potential field and the solution for a spherically-symmetric wind for the given base temperature, density, and polytropic index. The initial temperature, density, and velocity profiles are shown in Figure 1. The temperature curves appear irregular due to the small change in temperature over the relatively large radial range – a consequence of the polytropic index being near unity. Only three significant figures were retained after the calculation so what is seen here is essentially roundoff error.

Results for the steady-state solutions, given the above initial conditions, are ordered according to the four cases treated: (a) dipole, $\beta = 1.0$, (b) quadrupole, $\beta = 1.0$, (c) hexapole, $\beta = 1.0$, and (d) dipole, $\beta = 0.2$. The steady-state magnetic field geometries are shown in Figure 2. Here is seen the well-known property that the flow is nearly radial beyond 3–4 $R_\odot$. The streamers are those volumes which are

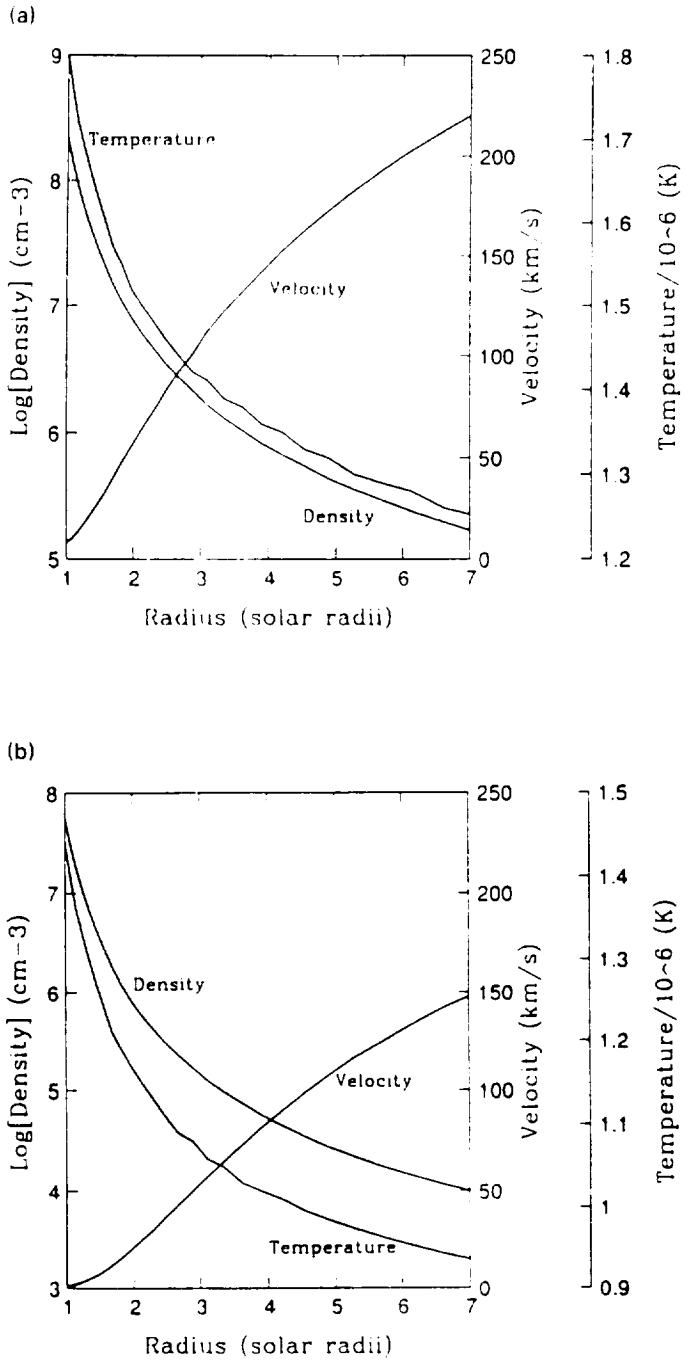

Fig. 1a–b. Density, temperature, and velocity profiles in radius of the initial ($t = 0$) state in the relaxation. (a) Profiles for the $\beta = 1.0$ cases. (b) Profiles for the $\beta = 0.2$ case. Note that, except for the velocity scales, the scales differ between the two panels. The irregularities in the temperature profiles are roundoff errors.

1.8
1.7
1.6
1.5
1.4
1.3
1.2
Temperature/10^6 (K)

1.5
1.4
1.3
1.2
1.1
1
0.9
Temperature/10^6 (K)

al ($t = 0$) state in the
ase. Note that, except
ities in the temperature

magnetically closed, and it is evident that relatively small volumes in the streamers remain magnetically closed in comparison to the initial states. These volumes are surrounded by a low-density shell but, as will be shown below, the densities in the large coronal hole-like open regions are otherwise only slightly lower than in the streamers. In each panel of Figure 2, four dotted lines are shown and labelled A, B, C, or D. These lines indicate the positions used to plot variables versus radius in Figures 3 and 4 below.

In displaying results for the physical variables, we will concentrate on the density and the velocity, these being the two variables that determine the Lα intensity. Other variables will only be shown when necessary for physical understanding. Figure 3 shows the density variation in the radial directions labelled in Figure 2. These plots show the relative density – the density divided by the density plotted in Figure 1. Thus, it measures the change in density with respect to a spherical flow profile. Curves D in Figures 3(a), 3(c), and 3(d), and curve C in Figure 3(b) are all profiles cutting through the cores of streamers. It is seen that there is a density enhancement in the core ranging from ≈75% for the low β dipole down to 20% for the equatorial streamer in the hexapole. On the flanks of streamers, for example as shown by curve C in Figure 1(a), there is a density deficit. Nevertheless, in the centers of open regions, the density deficit is always less than ≈20%. This is an important point to note in applying this specific model to computing Lα intensities, and we will return to it later. Also apparent in this figure, and the ones that follow showing variation of other variables with radius, is a rapid fluctuation from one grid point to the next for the first two or three points above the base. This is a consequence of the type of extrapolation used to determine those variables at the boundary which are calculated from the interior solution instead of fixed by the boundary conditions (Wang *et al.*, 1992, 1993; Steinolfson, Suess, and Wu, 1982). The phenomenon has no significant effect on the solution above the fourth grid point and, in particular, no effect above 1.2 $R_\odot$ – the minimum radius UVCS can observe.

Figure 4 shows the radial velocity along the directions labelled in Figure 2. In addition, the initial state profile is plotted as a dashed line – the same profile as shown in Figure 1. The flow speed is, except for numerical diffusion, identically zero in the streamers. This is obvious from curves D in Figures 4(a), 4(c), and 4(d), and curve C in Figure 4(b). Above the streamers, the velocity is greatly reduced. However, away from the streamers, whether in the center or at the edges of open regions, the flow speed differs little from the initial state.

Taken together, the density and flow speed illustrate that this is not a constant mass flux model – the flow speed at the base varies with polar angle. Therefore, these results appear somewhat different than might be anticipated based on intuition gained from, for example, the calculation by Kopp and Holzer (1976). A rapidly diverging magnetic field does not necessarily lead to a low density and high velocity flow – depending also on whether the rapid divergence occurs below or above the sonic critical point. So, on the flanks of streamers, where rapid field line divergence

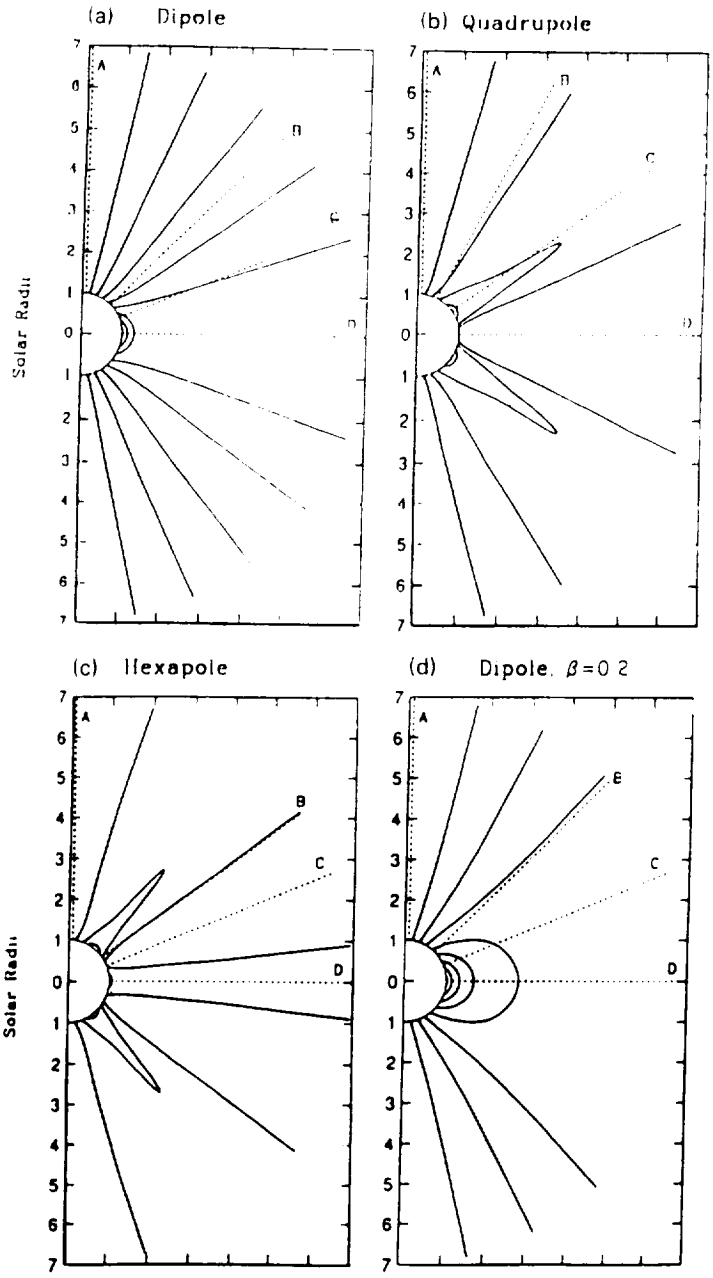

Fig. 2a–d. Magnetic field line plots for the four cases: (a) dipole, $\beta = 1.0$, (b) quadrupole, $\beta = 1.0$, (c) hexapole, $\beta = 1.0$, and (d) dipole, $\beta = 0.2$. The relaxation times allowed to reach these equilibria are: (a) 22.22 hours, (b) 16.67 hours, (c) 18.06 hours, (d) 19.44 hours. In each panel, four dotted lines are labelled 'A, B, C, or D'. These show the radial directions used for plotting certain variables vs radius in succeeding figures. Thus, the quadrupole in plot (b) will have these variables plotted vs radius at the pole (A), at the edge of the polar open region (B), through the mid-latitude streamer (C), and along the middle of the equatorial open region (D).

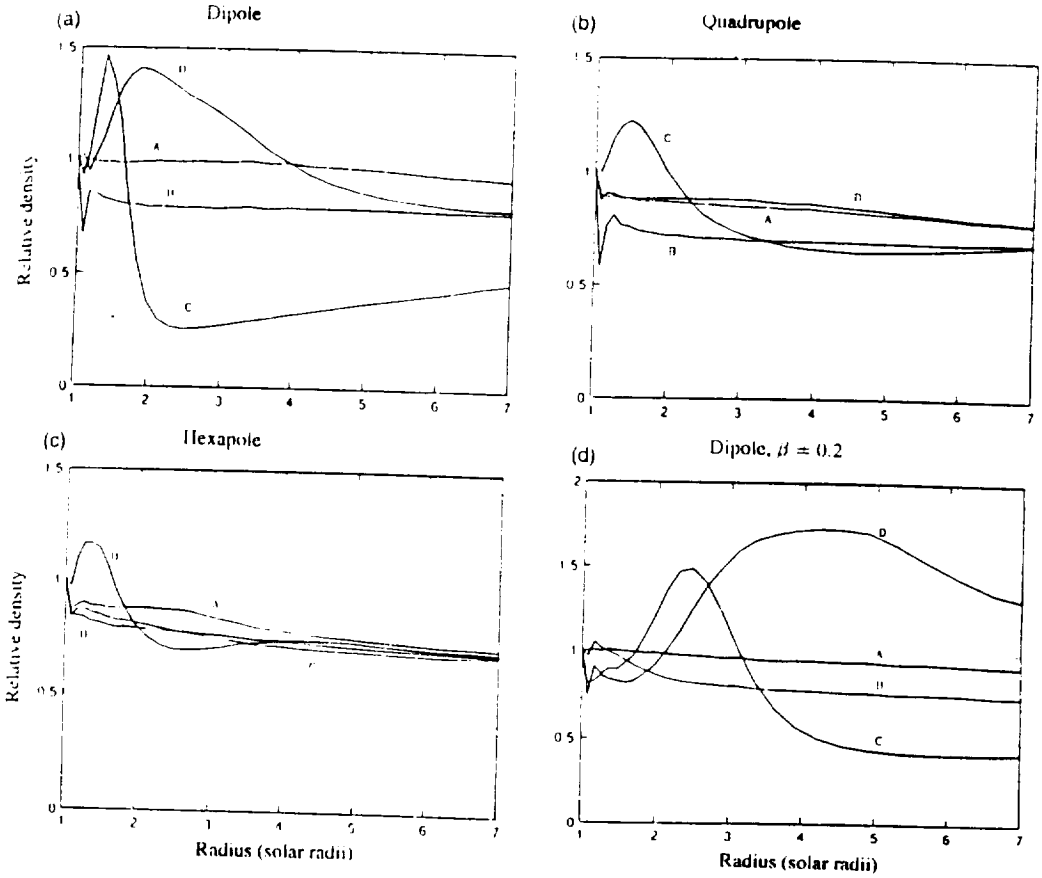

Fig. 3a–d. Density as a function of radius. Each panel is for the corresponding case in Figure 2. The curves are plotted along the directions shown in Figure 2. For example, the four curves in (c), labelled 'A, B, C, D', are along the four directions shown in Figure 2(c) and labelled in the same manner. Densities in each curve have been normalized to their values in the initial profile (Figure 1(a) for (a–c), and Figure 1(b) for case (d)). Hence, a density enhancement is indicated by values greater than unity, and *vice versa*. The density concentrations in the streamers are clearly visible, generally being on the order of 25% to 50% above the initial state.

occurs over a narrow range, the density does become small (as in Figure 3(a), curve C) but the flow speed never gets large (as in Figure 4(a), curve C). The other important thing to note is that the cusp (top of the streamer) in the $\beta = 0.2$ dipole lies at about 6 $R_\odot$. This seems large enough to cover the range of streamer heights expected in the solar corona and therefore we will not concern ourselves with computing models for smaller β-values.

A more complete picture of the behavior of the density can be gained by also considering plots of the density versus polar angle at different heights. These are shown in Figure 5, where each curve is labelled with the heliocentric distance it represents (e.g., 2.30 $R_\odot$ is at 2.30 $R_\odot$). Figure 5(a), the $\beta = 1.0$ dipole, shows the density enhancement in the streamer (polar angle of 90°), the deficit in the adjacent

ole, $\beta = 1.0$.
se equilibria
. four dotted
ain variables
es plotted vs
streamer (C).

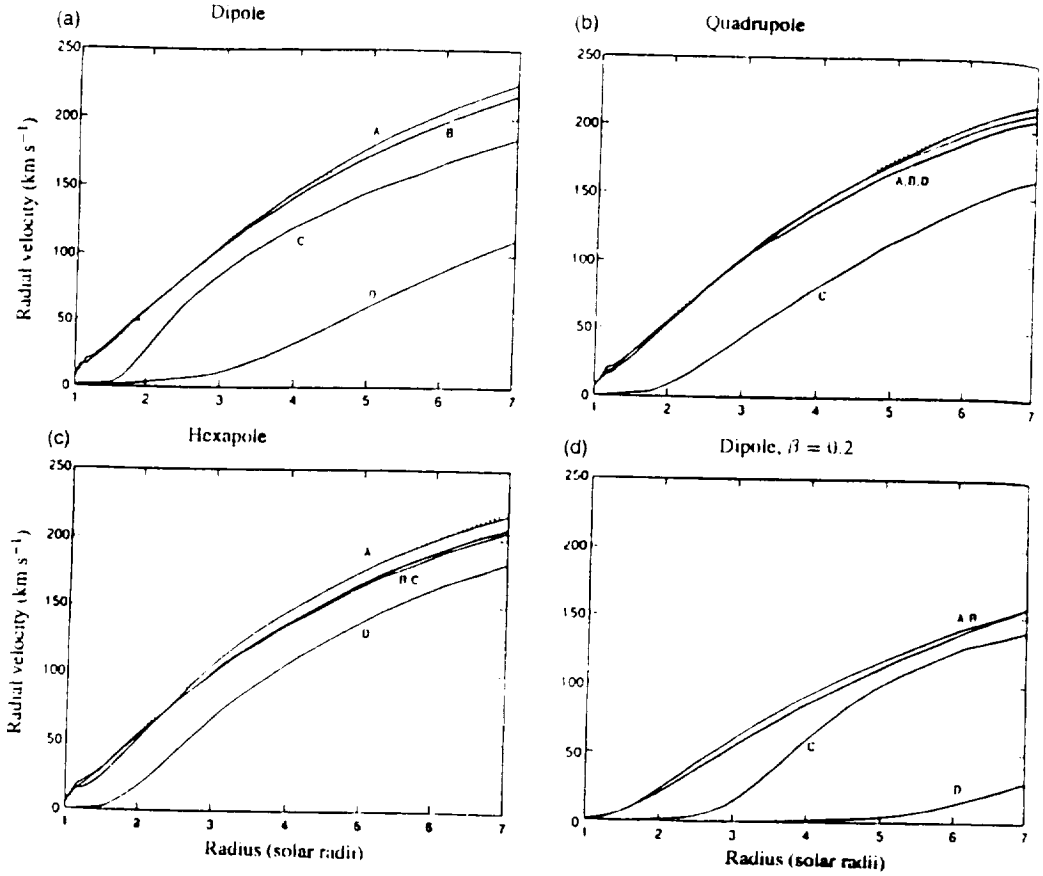

Fig. 4a–d. Radial velocity as a function of radius. Each panel is for the corresponding case in Figure 2. The curves are plotted along the directions shown in Figure 2. For example, the four curves in (c), labelled 'A, B, C, D', are along the four directions shown in Figure 2(c) and labelled in the same manner. The dotted line in these plots is the $t = 0$ profile, the same as shown in Figures 1(a) and 1(b).

trough, and the large plateau of density that is only a small amount less than in the streamer and extending throughout the open region beyond the trough. The behavior of the density around the mid-latitude streamer in the quadrupole, and around the mid-latitude and equatorial streamers in the hexapole is very similar. The only difference for the $\beta = 0.2$ dipole is that the troughs are considerably broader.

The broad, high density plateau in the open region is distinctly unlike a coronal hole. The reason for this is that in this model no effort has been made to generate the high coronal hole flow speeds that lead to low densities. Suess *et al.* (1977) have shown in a similar model that a temperature increase of 50% or more at the center of the open region is necessary in a polytropic model such as this to produce densities like those that are observed in coronal holes.

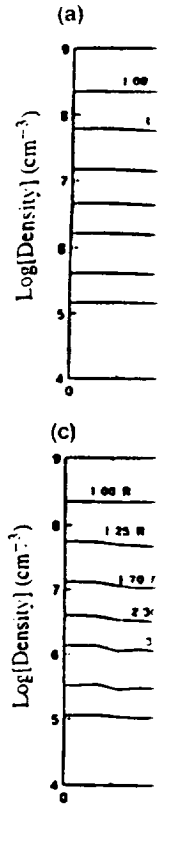

Fig. 5a–d.
labelled acc
the density
are flat. Abo
trough in de
to what it w
smaller, as
the base. To
required an
otherwise st

Figure
Figure 5.
whose he
while the
streamers
the open
humps on
These

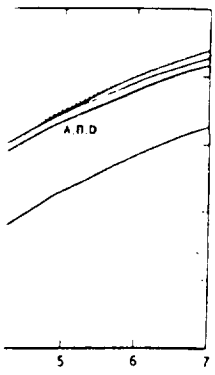

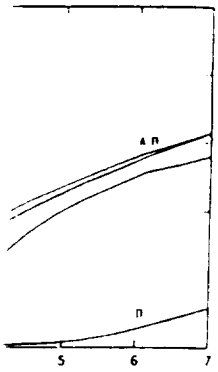

ar radii)

esponding case in
le, the four curves
nd labelled in the
vn in Figures 1(a)

nt less than in
he trough. The
quadrupole, and
is very similar.
re considerably

nlike a coronal
ade to generate
s *et al.* (1977)
or more at the
this to produce

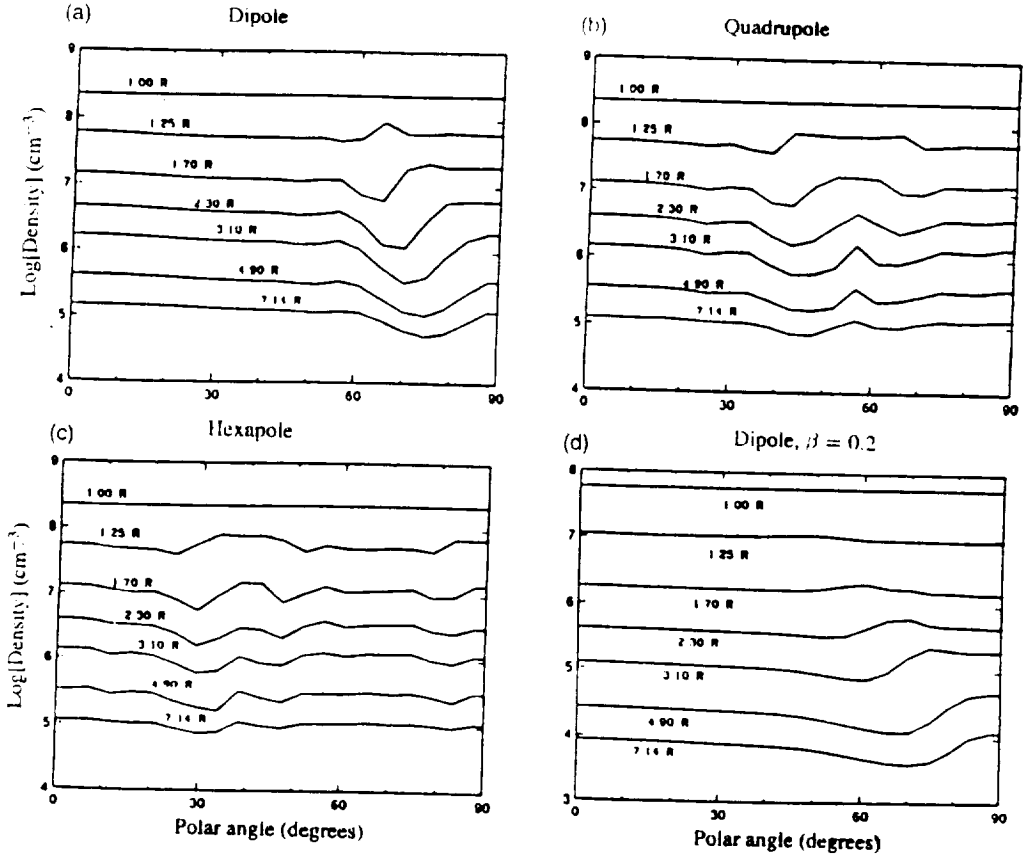

Fig. 5a–d. Density vs polar angle, between the pole (0°) and the equator (90°). Each of the curves is labelled according to the heliocentric distance it refers to. Thus, the curve labelled 1.70 R indicates the density at 1.70 $R_\odot$ heliocentric radius. The density at the base is constant and so the curves there are flat. Above the base, there is a small density enhancement in the streamer (ca. 5% to 50%) and a trough in density at the edge of the streamer. In the middle of the open region, the density is very close to what it was in the initial state (see also Figures 3(a–d)). The reason it is not an order of magnitude smaller, as in an observed coronal hole, is that we have used constant temperature and density at the base. To produce a true coronal-hole-like profile in a polytropic model such as this would have required an increase in the temperature at the base of the open region (Suess *et al.*, 1977). Unless otherwise stated $\beta = 1.0$.

Figure 6 shows the radial velocity plotted in the same manner as the density in Figure 5. The velocity is again seen to be essentially zero inside the streamer(s), whose height decreases rapidly with increasing magnetic field complexity. Thus, while the $\beta = 1.0$ dipole streamer extends to 3 $R_\odot$, neither of the $\beta = 1.0$ hexapole streamers reaches beyond 1.70 $R_\odot$. As indicated above, the flow speed throughout the open region is very similar to the initial state flow speed, excepting for small humps on the flanks of the streamers.

These four models constitute the basis for the calculation of Lα intensities.

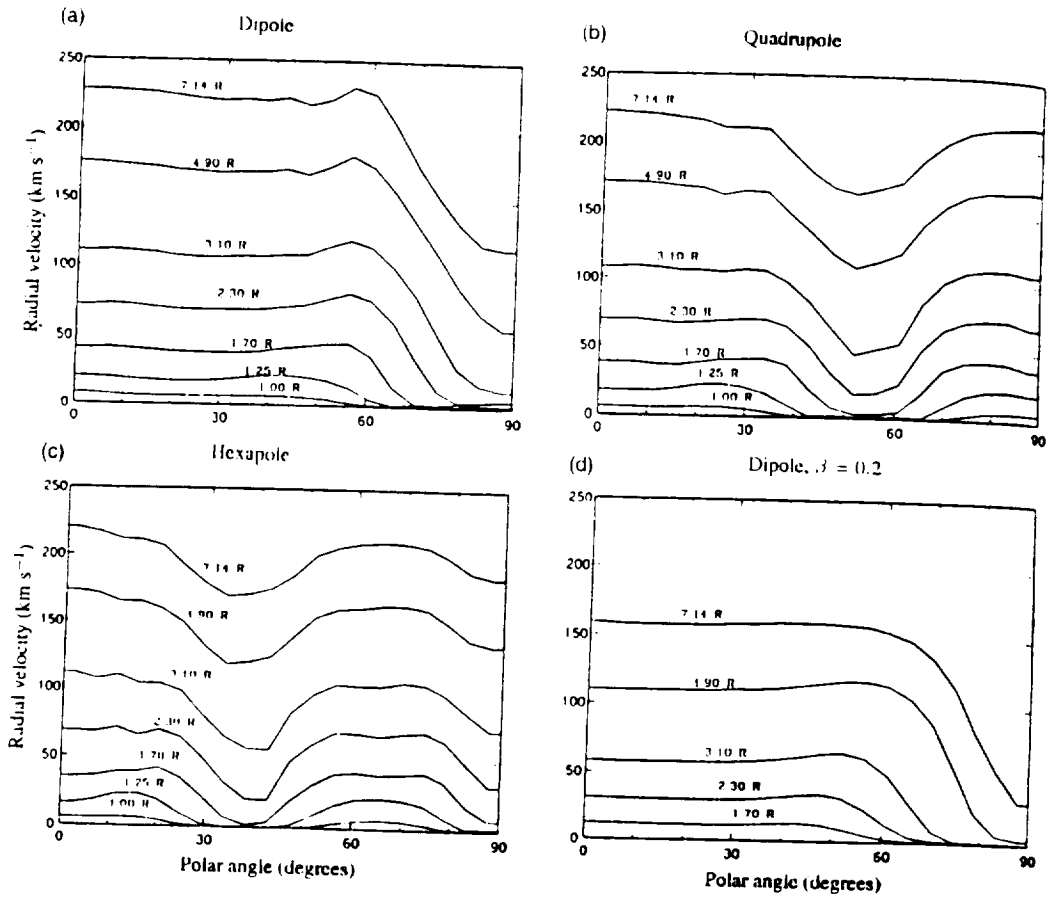

Fig. 6a–d. Radial velocity versus polar angle, between the pole and the equator. Each curve, plotted for different heliocentric distance, is labelled in the same manner as in Figures 5(a–d). The velocity in the magnetically closed regions is essentially zero. The reason it is not identically zero is that there is a small amount of numerical diffusion – quite small, as indicated by the velocity less than 10 km s^{-1} inside the $\beta = 1.0$ dipole streamer at 2.30 $R_\odot$ (top left panel).

In using them, we progress from a straightforward calculation of the intensity measured when viewing the streamer as seen in Figure 2 (i.e., from a position in the magnetic equatorial plane) to other viewing positions and to approximations based on the models. A comparison with intensities from observed streamers is used to guide suggestions for further development of the model by illustrating specific weaknesses in the present four models. We will conclude that a satisfactory physical model of streamers, for the purpose of computing expected UVCS Lα intensities, can be constructed through the application of the present simulation with an appropriate choice of boundary conditions to better represent the dynamics of the solar wind in the open magnetic field regions. This is well within the capabilities of the simulation and will constitute the next stage of this project.

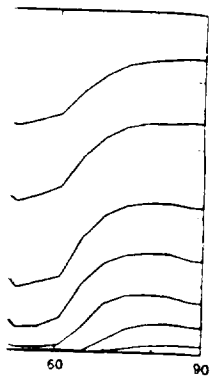

0.2

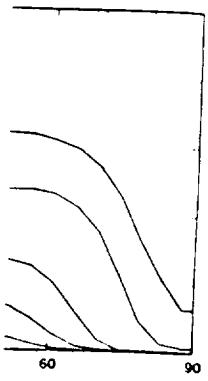

:rees)

ich curve, plotted
l). The velocity in
ero is that there is
s than 10 km s^{-1}

f the intensity
n a position in
pproximations
ved streamers
by illustrating
t a satisfactory
ed UVCS Lα
imulation with
e dynamics of
he capabilities

3. Predicted vs Observed Densities

As mentioned in the Introduction, density is the only physical quantity in streamers to be even partially measured. Coronagraph images usually are polarization brightness (pB) images. Because pB is proportional to the line-of-sight integral of the density times a scattering function (Billings, 1966), it is possible from pB images to derive density maps. Usually, this procedure is performed with the Van de Hulst method (1950): that is, the density distribution is supposed to be cylindrically symmetric.

This technique has been used to derive densities from eclipse observations of streamers. Dollfus, Laffineur, and Mouradian (1974) derived densities for a number of streamers observed in the eclipse of February 15, 1961, and compared their values with those pertaining to 13 different streamers, which represent all results published between 1952 and 1972. From this, as well as from a comparison between values derived by different authors for the same streamer, these authors conclude that different determinations for the same structure agree only within a factor 2 and different structures may have densities which differ, at the same altitude, by a factor 10, even in streamers observed at the same eclipse, that is, independently of the epoch of the solar cycle. All densities refer to the streamer axis; Dollfus *et al.* assumed that streamers are axially symmetric and that the distribution of density, in the direction normal to the streamer's axis, is somehow intermediate between being uniform and having a gaussian distribution. Different assumptions on the streamer geometry, or on the distribution of density across a streamer, may possibly explain some of the discrepancies in the values derived for the same structure.

Densities predicted by a theoretical model have to comply with this rather loose observational constraint. Figure 7 gives, on the left panel, the behavior of the density predicted by our model along the axis of equatorial streamers, for dipolar and hexapolar configurations in the case of $\beta = 1.0$, and for dipolar geometry only in the low β ($\beta = 0.2$) case. Densities along the axis of off-equator streamers, both in the quadrupolar and hexapolar geometries, are approximately equal to those along the axis of equatorial streamers and are not shown. In the right panel, we present a figure made up from Figures 16(a–b) of Dollfus *et al.*, which shows, besides all density determinations in streamers between 1952 and 1972, the values derived by Dollfus *et al.* for four different streamers observed in the eclipse of 1961.

The $\beta = 1.0$ curves, cutting through the bundles of curves shown in the right panel, represent correctly the observed densities. As we said, it is not possible to establish, from the data published so far, any trend in the different behavior of individual streamers. For instance, contrary to expectations, the streamer closest to the equator in Dollfus *et al.*'s data (position angle 95°), has lower densities than a mid-latitude streamer (position angle 55°) and the highest densities among those from published results 1952–1972 pertain to a streamer observed close to

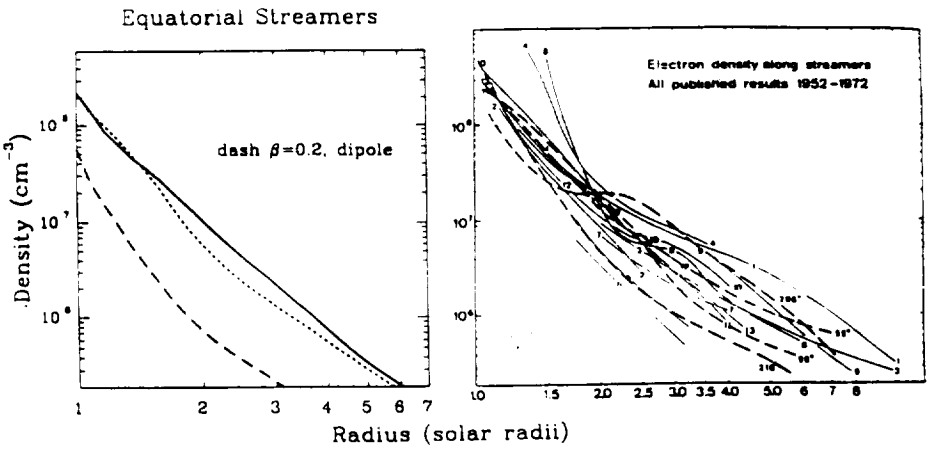

Fig. 7. *Left*: density vs height profiles along the axis of equatorial streamers in dipolar ($\beta = 1.0$ – solid line – and $\beta = 0.2$) and hexapolar geometries as derived from Wang *et al.*'s (1992, 1993) models. *Right*: densities along streamers from all results published between 1952 and 1972 (labels 1–13, solid lines) and along 4 streamers observed at the February 15, 1961 eclipse (dashed lines, labelled by their position angles). See Figures 16(a–b) of Dollfus, Laffineur, and Mouradian (1974) for further information on this panel.

the activity minimum (curve 4, February 5, 1962 eclipse). Hence, we can only conclude that the $\beta = 1.0$ curves are *consistent* with observed density profiles in coronal streamers. This conclusion is confirmed by a comparison of the radial density distribution predicted by our model with densities derived from Clark Lake Radioheliograph streamer observations (Gopalswamy, Kundu, and Szabo, 1987). This comparison is limited to the lower corona, at heights below and near 2 $R_\odot$, and shows (Figure 8) how our predicted density profile lies between densities derived from fundamental and harmonic plasma hypotheses. Finally, we notice that the lack of a definite observational difference between low and high latitude streamers, agrees with predictions from our model.

On the other hand, by comparing the two panels of Figure 7, we conclude that our $\beta = 0.2$ case is not realistic because densities are too low and the cusp is far too high. Nevertheless, the $\beta = 0.2$ curve shows a marked change in its slope that is not so evident in the $\beta = 1.0$ hexapole streamer, and is altogether absent in the $\beta = 1.0$ dipole streamer, which may reproduce the behavior shown by some of the observed structures. To recover this break in the density profile at higher β probably requires changing conditions outside the streamer. A change in the density gradient of the observed profiles has, in fact, been interpreted in terms of a different behavior of this physical parameter in the region of the streamer's helmets (Dollfus *et al.*, 1974). Obviously, the present simulations do not allow us to predict whether the resulting curve will be capable of reproducing some of the observed density profiles more closely than the high β curve. However, it is likely that structures with differing cusp heights correspond to different β values (Steinolfson, Suess,

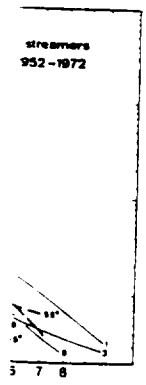

lipolar (β = 1.0
L.'s (1992, 1993)
and 1972 (labels
se (dashed lines,
louradian (1974)

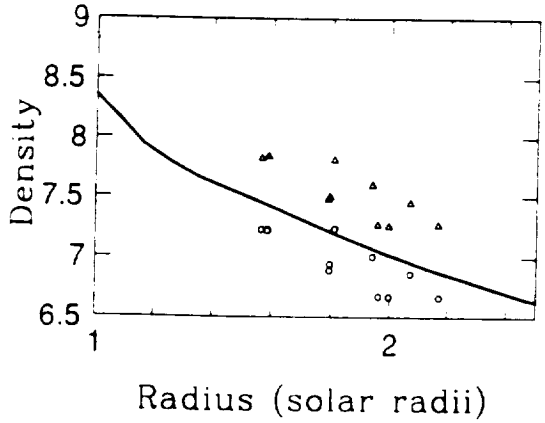

Fig. 8. Predicted density vs height profile along the axis of the equatorial streamer in the case of high β (β = 1.0) dipolar configuration (solid line) and density determination from radio observations of a streamer obtained on July 27, September 12 and 17, 1985: o represent values of density derived from the hypothesis of fundamental plasma emission, △ represent values of density derived from the hypothesis of harmonic plasma emission.

we can only
nsity profiles
of the radial
m Clark Lake
Szabo, 1987).
ear 2 $R_\odot$, and
sities derived
otice that the
de streamers,

conclude that
he cusp is far
its slope that
ther absent in
nown by some
ile at higher β
e in the density
s of a different
mets (Dollfus
edict whether
erved density
nat structures
olfson, Suess,

and Wu, 1982). We conclude that the comparison between model-predicted and observed density profiles points to the need for a thorough analysis of the effect of different boundary conditions in and around streamers on the resulting density profiles.

In the following section we proceed to evaluate the Lα emission in streamers adopting the β = 1.0 models.

4. Lα Emission from Streamers

The formation of the Lα line in the solar corona has been discussed by a number of authors (Gabriel, 1971; Beckers and Chipman, 1974; Withbroe *et al.*, 1982; Noci, Kohl, and Withbroe, 1987) who showed how coronal Lα observations can be used as a diagnostic tool to determine coronal densities, temperatures, and outflow velocities. Although, at coronal temperatures, only ≈1 proton in 10^7 is tied up in neutral hydrogen, the strongest component of the coronal Lα is due to the scattering of chromospheric Lα photons by neutral hydrogen atoms. An electron scattered component, produced by Thomson scattering of Lα radiation, is about three orders of magnitude weaker than the resonantly scattered component and will be ignored in the following.

The total (i.e., integrated over the line profile) Lα intensity, as observed along the direction **n** is given by

$$I = \frac{hB_{12}\lambda_0}{4\pi} \int_{-\infty}^{\infty} N_1 \, \mathrm{d}x \int_{\Omega} p(\varphi) \, \mathrm{d}\omega' \int_{0}^{\infty} I_{\mathrm{chrom}}(\lambda, \mathbf{n}') \Phi(\lambda - \lambda_0) \, \mathrm{d}\lambda \,. \qquad (1)$$

where h is the Planck constant, B_{12} the Einstein coefficient for the line, λ_0 the rest value for the central wavelength λ of the Lα transition, and N_1 the number density of hydrogen atoms in the ground level; the unit vector $\mathbf{n}$ is along the line of sight x and the unit vector $\mathbf{n}'$ is along the direction of the incident radiation; $p(\varphi)\,\mathrm{d}\omega'$ – where ω' is the solid angle around $\mathbf{n}'$ – is the probability that a photon travelling along the direction $\mathbf{n}$ was travelling, before scattering, along the direction $\mathbf{n}'$; Ω is the solid angle subtended by the chromosphere at the point of scattering; I_{chrom} is the exciting chromospheric radiation and Φ is the coronal absorption profile. In the following we assume that the intensity of the chromospheric Lα radiation is constant across the solar disk and that the velocity distribution of the scattering hydrogen atoms is Maxwellian. The dependence of the Lα scattering process on the angle has been taken from Beckers and Chipman (1974) and we adopted the value given by Gabriel (1971) for the ratio between the neutral hydrogen density and the proton density at different temperatures (because of the low coronal density all hydrogen atoms are assumed to be in the ground level, therefore $N_{\mathrm{H}}/N_p = N_1/N_p$). This is not entirely correct, since temperatures in our model are 'effective' temperatures, resulting from the polytropic index used in the energy equation. We will come back to this point in Section 6.

In order to evaluate the Lα intensity in coronal streamers from Equation (1), we need to know how streamers extend in the third dimension. Because our models are axisymmetric, it is realistic to assume that they give the distribution of physical parameters in a meridional plane, identified with the plane of the sky and normal to the line of sight. If we focus on the dipolar model, we recognize that its geometrical configuration is highly reminiscent of the conditions observed at solar minimum, when streamers are concentrated along the equator. Therefore, as a first hypothesis, we assume that streamers extend all the way around the equator, in a continuous belt, and calculate, on the basis of Equation (1), the radial distribution of Lα intensity in a dipolar geometry. To this end, in the following, densities along the line of sight are considered equal to those given by the model at the same latitude and radial distance. Figure 9 gives the radial profile (solid line) of the Lα intensity, evaluated along the streamer axis (which, in a dipolar geometry, lies in the equatorial plane) up to a height of 4.5 $R_\odot$. Values at larger distances are not given, since, beyond that height, field lines are open and the Lα brightness would no longer originate in the streamer. Moreover, open-field regions are not described realistically in our simulations, their density being definitely overestimated (see Wang *et al.*, 1992, 1993, for further comments on this point). This is apparent also from the slope of the intensity vs distance curve, which keeps constant over all the computational domain as if densities decrease linearly with distance. This is unexpected, as the line of sight, in regions close to the cusp height and beyond it, crosses mostly through the low-density open-field regions. Altogether, the slope of the Lα intensity gradient predicted in the case of a continuous belt of streamers circling the Sun, is open to criticism.

The inaccuracy of the brightness vs distance profile may be ascribed both to

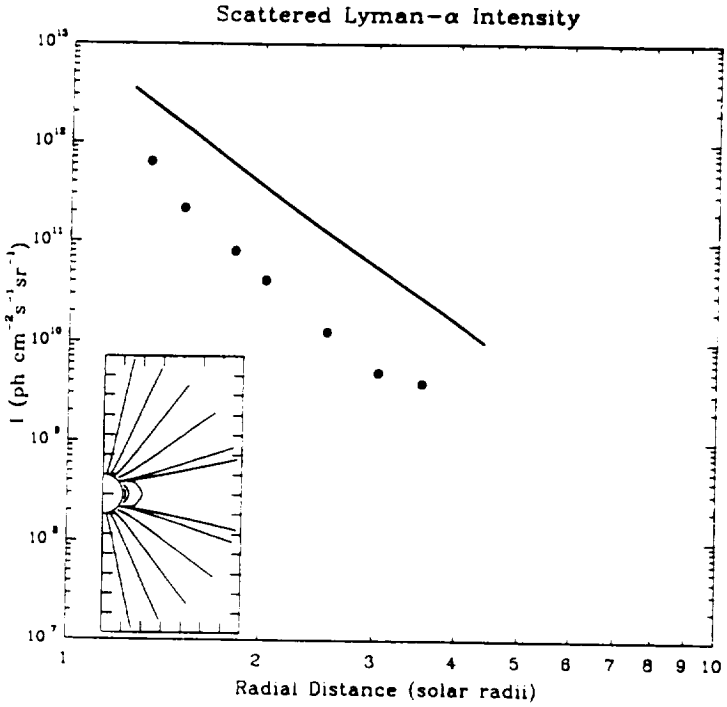

Fig. 9. Predicted Lα intensity vs radial distance along the axis of an equatorial streamer in a dipolar geometry, for a plasma $\beta = 1.0$ (solid line). The streamer is assumed to extend all the way around the equator, and the calculation is performed up to a height of 4 $R_\odot$, as at higher altitudes most of the contribution to Lα intensities will come from open regions. Results from rocket observations of Lα intensities from a quiet coronal region are also shown (dots).

an incorrect treatment of the open field region and to an inappropriate geometry. The latter factor would be influential if only the slope at large distances is wrong. However, the values of the Lα intensity at low heights also look too high, in comparison with the few data points available so far. In Figure 9 we show (dots) the Lα intensities given in Figure 6-1 of the UVCS Science Requirement Document: these data refer to a quiet region and were obtained in 1979 during a rocket flight (Kohl *et al.*, 1980). Because they do not refer to a streamer, they do not provide any information about the change in the slope of the Lα intensity gradient in the cusp region, but we can infer that Lα streamers would be a few times brighter than appears from the rocket data. The Lα brightness predicted from the model is about one order of magnitude larger than observed in quiet regions, which, taking into account that our densities are realistic, is too large a factor. This rules out our initial hypothesis of a continuous belt of streamers circling the solar equator. It is worth pointing out that our conclusion is consistent with observations, as these seem to indicate the presence of several streamers spread, at a given latitude, over different longitudes (Dollfus, private communication).

From this analysis we conclude that we need both a better simulation of open

field regions and a definition of the streamer geometry through a full 3-D model. However, we may still get realistic predictions by adopting *a priori* the streamer configuration and neglecting the contribution from the outer low-density regions. The resulting profiles of intensity vs distance will illustrate the behavior of the Lα brightness for different geometries and UVCS data will eventually allow us to identify the more realistic configurations.

Figure 10 shows the Lα intensity vs distance profiles assuming three different streamer configurations in a direction normal to the streamer axis and parallel to the line of sight (we remind the reader that streamers are supposed to lie in a meridional plane). Either the *angular* width of a streamer is constant with height (fan-shaped streamer) and equal to its base angular width (as seen in the plane of the sky) or its *linear* width is constant with height (constant-thickness streamer) and equal to the distance between the footpoints of the highest closed field lines (as seen in the plane of the sky) or streamers are 'cone-shaped' structures and therefore have a width, initially equal to that of a constant-thickness streamer, which decreases linearly with height up to the cone vertex, identified with the streamer's cusp. Figure 10 shows that, in a dipolar geometry, an equatorial fan-shaped streamer differs negligibly from a continuous belt of streamers circling the Sun. This is due to the large width of the streamer (half width $\approx 38°$): outer regions contribute to the emergent intensities only at great distances where densities are too low to affect significantly the Lα brightness. As a consequence, unless future observations will show streamers to be brighter than assumed so far, we are led to discard the hypothesis of streamers as constant angular width structures. On the contrary, constant thickness and cone-shaped streamer structures lie close enough to the observed data points to be equally plausible.

However, our model locates the cusp only approximately, both because our model does not take diffusive effects into account and because of the coarse resolution of our mesh points. Hence, in order to illustrate, in a cone-shaped geometry, how different cusp altitudes affect the Lα intensity gradient, we have considered the cusp height as a free parameter and evaluated the resulting radial profiles in the usual dipolar geometry and high β plasma. Figure 11 shows the Lα intensity vs distance profiles for a cone-shaped streamer whose vertex – i.e., cusp height – is located at altitudes ranging between 2.5 and 6 $R_\odot$. We point out that such a large variation in the position of the streamer's cusp far exceeds the uncertainty of the model and is shown only for display purposes (although the procedure is not entirely consistent, as different β values would be required to build models with such different cusp heights). We conclude that the Lα intensity and the slope of the Lα intensity gradient initially (i.e., close to the Sun) depend only weakly on the shape of the streamer, but, at large distances, are dictated by the streamer's 3-D structure and, in the case of a cone-shaped feature, by its cusp height.

So far, our examples referred to a global dipolar streamer. However, our results can be extended to the quadrupolar and hexapolar model configurations by taking into account the differences in the streamer geometry. As we have shown in Sec-

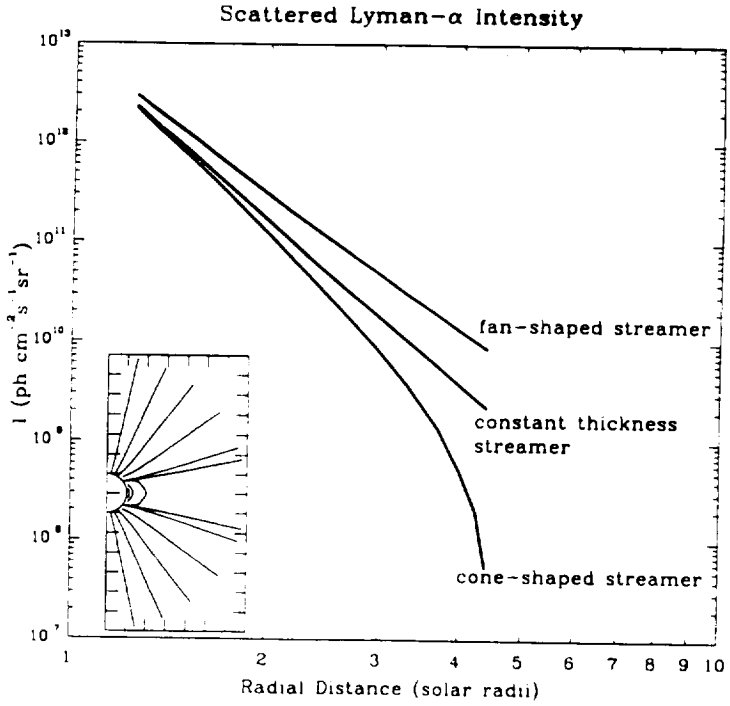

Fig. 10. Predicted Lα intensity vs radial distance along the axis of an equatorial streamer in a dipolar geometry, for a plasma $\beta = 1.0$. The streamer thickness in a direction normal to the plane of the sky is assumed either to have a constant angular width (fan-shaped streamer) equal to its angular base width (≈76°) or to be constant with height (constant thickness streamer) and equal to its base width (≈1 $R_\odot$) or to decrease linearly with height (cone-shaped streamer) up to the cusp height ($R_{cusp} = 4.5\ R_\odot$).

tion 3, densities are about equal in low and high latitude streamers. Therefore, the Lα brightness from these features turns out to scale, with respect to that originating in a dipolar equatorial configuration, in the same proportion as the streamer thickness. The Lα brightness from an equatorial hexapolar streamer, for instance, will be a factor 2–3 smaller than that from an equatorial dipolar streamer and about equal to the brightness from the high-latitude hexapolar streamer.

We did not consider, yet, the case of off-axis observations, which should provide a more comprehensive test of the model by allowing us to determine the physical parameters of the streamer *across* its axis, over a meridional plane. For instance, if SOHO UVCS were to observe an equatorial streamer – symmetrical with respect to a meridional plane through its axis – when its symmetry plane lies in the plane of the sky, it should be possible, via off-equator observations, to check the shape and physical parameters of the streamer in the meridional plane purportedly described by the model.

Figure 12 gives the Lα intensity gradient, measured in the plane of the sky along directions parallel to the axis of the streamer, for the usual dipolar configuration

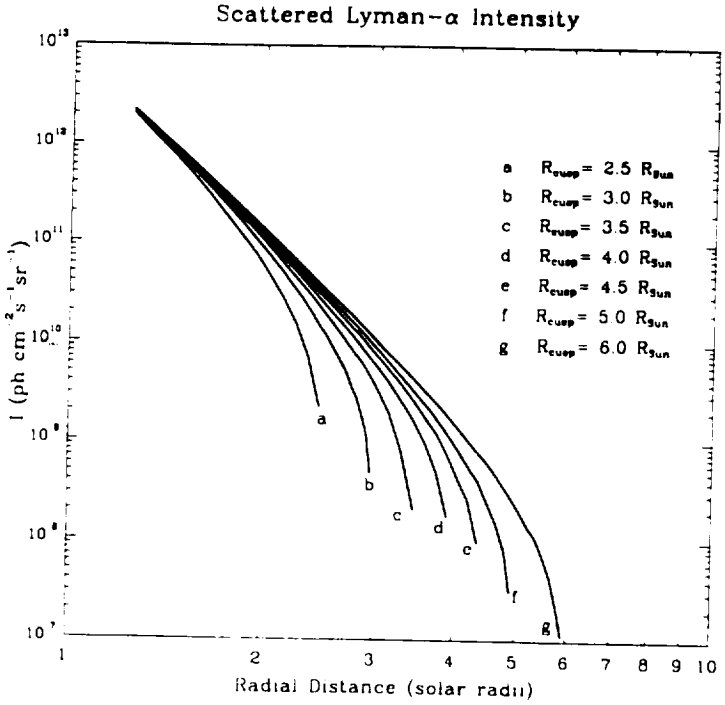

Fig. 11. Predicted Lα intensity vs radial distance along the axis of an equatorial streamer in a dipolar geometry, for a plasma $\beta = 1.0$. The streamer cusp is assumed to be located at different heights ranging from 2.5 to 6 $R_\odot$.

($\beta = 1.0$, $R_{cusp} = 4.5\ R_\odot$), in the hypothesis of a cone-shaped structure. The Lα intensity vs distance gradient is here dictated by the variation of density across the streamer and by the decrease of the integration length along the line of sight, as we move off the equatorial plane. The latter factor is responsible for the intensity drop which occurs at increasingly lower distances, as we move to larger offsets, and mimics the behavior observed in the cusp region in the equatorial plane, also shown in the figure.

If we now move in the plane of the sky, along a direction normal to the streamer axis, and we evaluate the Lα intensity at increasing offsets, we would guess that the Lα brightness decreases proportionally to the decrease in the integration length, and that, as a consequence, the ratio of Lα intensities evaluated at positions corresponding to increasing offsets can never be lower than the ratio between the corresponding integration lengths. For instance, at a distance – measured along the axis of the streamer – of 1.25 $R_\odot$, the intensity ratio $I_R = I_{L\alpha,\ 0.2\ R_\odot}/I_{L\alpha,\ 0.4\ R_\odot}$ is ≈1.5, while the ratio between the integration lengths at those offsets is ≈1.3. The decrease of density, as we move off axis, accounts for a 10% increase in the intensity ratio over the value predicted on the basis of the ratio between integration lengths. However, the intensity ratio is *smaller* than the ratio between integration

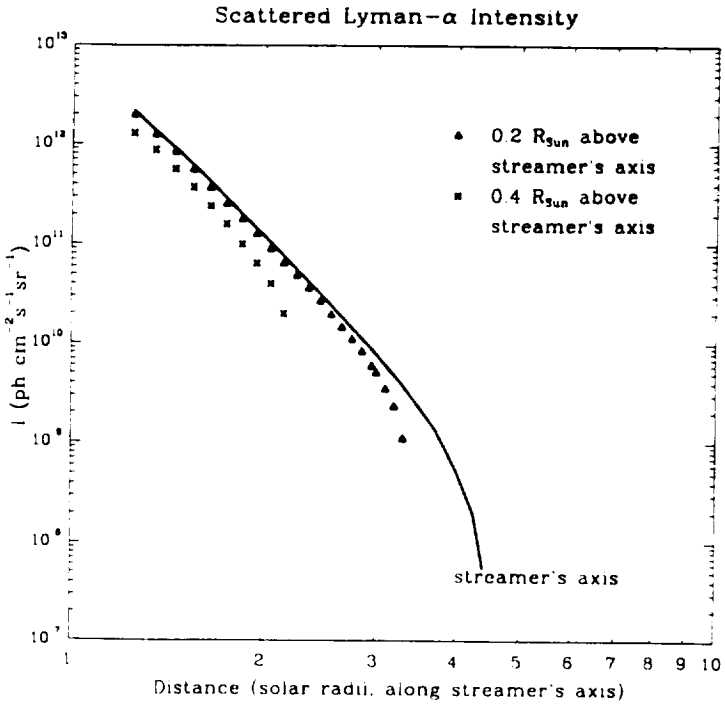

Fig. 12. Predicted Lα intensity vs distance (measured along the axis of an equatorial streamer) for different off-equator offsets in a cone-shaped equatorial streamer: solid line, intensity along the axis of the streamer, zero offset; △, intensity for an offset of 0.2 $R_\odot$; ×, intensity for an offset of 0.4 $R_\odot$. As usual the configuration is dipolar, the base width is ≈38° and the cusp height is 4.5 $R_\odot$.

lengths whenever the shorter integration path, at a larger offset, runs either through the density enhancement at the edge of the streamer (see Figure 5), or through regions with a lower temperature (and, as a consequence, a higher percentage of neutral hydrogen atoms). At a distance of ≈2 $R_\odot$, this effect makes the intensity ratio about 10% *smaller* than the ratio between integration lengths. Thus, from Figure 12, we conclude that the ratio between Lα intensities, evaluated at the same distance (along the streamer's axis) and different offsets, is approximately equal to the ratio of the integration lengths. In the hypothesis of an axially-symmetric density distribution, we conclude that densities play a secondary role, with respect to the streamer's geometry, in determining the value of Lα off-equator intensities. As a consequence, we have to devise a different technique in order to be able to determine the off-axis behavior of densities in streamers. The next section deals with this point.

5. Lα Emission from a Rotating Streamer

The extended lifetime of SOHO makes it possible to observe streamers over a prolonged period of time as they are carried around by solar rotation. Hence, generally, the line of sight will cut through the structure obliquely and the angle between the streamer's axis and the integration path will vary from 0° to 90° as the streamer moves from the central to the limb meridian. When the line of sight cuts normally through the streamer, the region which is closest to the Sun and, therefore, has the highest density, is located at the streamer axis: as a consequence, the highest contribution to the emergent intensity comes from this region. On the contrary, when the line of sight cuts obliquely through the structure it may happen, depending on the angle between the line of sight and the streamer axis and on the axial vs transverse density gradient, that the highest contribution to the emergent intensity originates from a region at some distance from the streamer axis. *If* evolutionary effects are negligible – i.e., *if* streamers are stable throughout a period of time – we may use this effect to get information on the density profile in a direction *normal* to their axis and, through prolonged observations, eventually reconstitute their entire structure. In other words, for stable structures solar rotation allows us to see streamers under different perspectives and use tomographic techniques to obtain their 3-D configurations.

In the previous section, we assumed that the streamers footpoints were rooted at the same longitude. However, if streamers are rooted in active regions, it is likely that their footpoints are rooted at the same latitude – say, along the equator – inasmuch as positive and negative polarities tend to align along the east–west direction. Although our model seems inappropriate to deal with this case – since it is not realistic to have magnetic 'poles' along the solar equator – as long as we do not have a 3-D simulation it is plausible to focus on the streamer sector and adopt the representation provided by the model to describe streamers lying on the equatorial plane. This allows us to explore the capabilities of the tomographic technique, because, in this hypothesis, the model provides a complete description of the behavior of density along the line of sight (at least for on-axis observations). Hence, in the following, contrary to what has been hypothesized so far, the streamer is assumed to lie on the equatorial plane.

Figure 13 shows how individual elements along the line of sight contribute to the total Lα intensity measured in the equatorial plane at a distance of 1.25 $R_\odot$. When the streamer is at the limb (streamer longitude 90°), its axis lies in the plane of the sky and is perpendicular to the line of sight. Therefore, the element lying at 1.25 $R_\odot$ along the axis is the element closest to the observer and provides the highest contribution to the emergent intensity (top left panel of Figure 13). As the streamer is carried around by solar rotation, different elements, at some distance form the axis, become the major contributors to the total intensity. Figure 13 demonstrates the progressive shift of the element which most contributes to the emergent Lα intensity, as the streamer longitude changes by 30°. The bottom right

panel, for instance, shows that, when the streamer has rotated by 30° behind the plane of the sky, the highest contribution to the emergent intensity comes from the element at a distance of $\simeq 0.72\ R_\odot$ along the line of sight (distances along the line of sight are counted from the streamer axis). Thus, by taking an extended set of data, at different locations along the axis of the streamer and at different rotation angles, we eventually get a complete map of the density of the structure.

We do not give any further example of this technique as a more realistic choice of boundary conditions in the open-field regions will modify the distributions of Figure 13. We anticipate that a lower density in open-field areas will result in a steeper decline of the contribution from elements located outside, or at the outer edge of the streamer. This effect may help getting a density map with higher spatial resolution than otherwise possible. Although stable structures may be a minority within the streamer family, the example of Figure 13 shows that it is worth developing this methodology further, as a means for an observational determination of the 3-D streamer's structure.

6. Discussion and Conclusions

Our purpose has been twofold: to provide guidelines for UVCS observational sequences and to compare our simulations with the scanty data available in order to guide further development of the numerical model toward more realistic global configurations.

The first objective has been reached, insofar as we have presented a set of predicted profiles of Lα intensity vs distance, both for on-axis and for off-axis observations and for different rotation angles of the streamer. These profiles can be easily adapted to different magnetic configurations. On the basis of our model for an axially-symmetric structure, we also show that off-axis observations allow an identification of the streamer's dimension along the line of sight. Finally, we have shown that this capability, combined with prolonged observations of a stable streamer at different longitudes, leads to a 3-D map of densities in streamers for comparison with our global simulation.

The model uses a polytropic relationship between density and pressure, rather than a full energy equation. Hence, the temperatures we predict are *effective* temperatures. Observationally, the Lα brightness depends on the electron temperature, via the neutral hydrogen abundance, and on the kinetic temperature, via the coronal absorption profile. As long as we consider integrated Lα brightness, the effect of an incorrect absorption profile is probably negligible. Model temperatures are, however, lower than temperatures derived from streamer observations (Liebenberg, Bessey, and Watson, 1975), so we apparently overestimate the neutral hydrogen abundance. Nevertheless, measured temperatures in streamers have such great uncertainty that we cannot resolve this issue until UVCS provides accurate measurements of the electron temperature.

Ultimately, our second objective is the more relevant. The simulations point

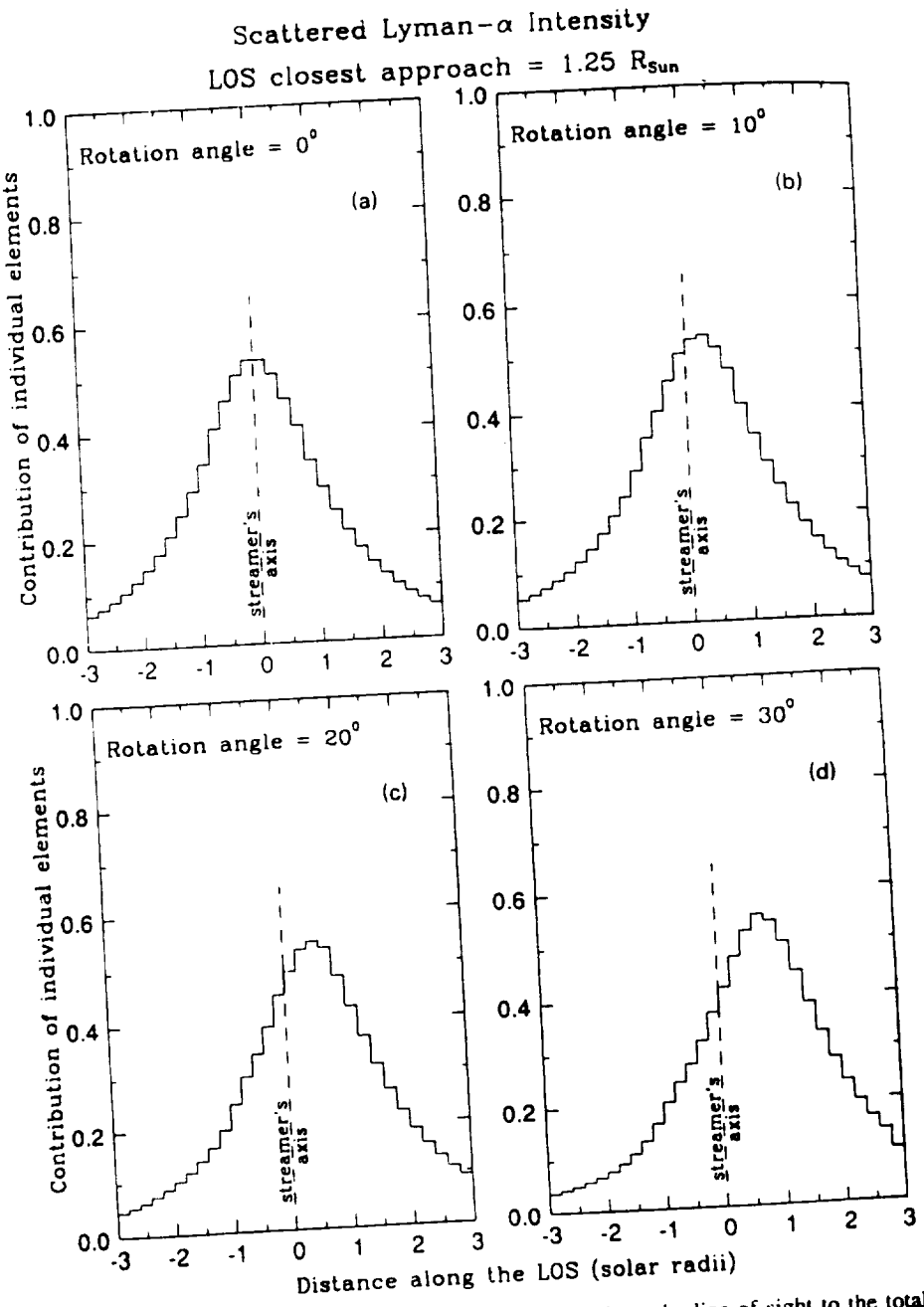

Fig. 13a–d. Predicted contribution of individual elements along the line of sight to the total Lα intensity from the usual dipolar, $\beta = 1.0$ streamer, supposed to lie in the equatorial plane, as a function of their distance along the line of sight. Negative (positive) distances are away from (towards) the observer, as measured with respect to the axis of the streamer. The line of sight intersects the plane of the sky at a distance of 1.25 $R_\odot$ and cuts obliquely through the streamer, unless the streamer axis is in the plane of the sky (streamer longitude: 90°). The contribution of individual elements to the total intensity is shown for: (a) streamer axis in the plane of the sky (rotation angle: 0°), (b) streamer at a longitude of 100° (rotation angle: 10°), (c) streamer at a longitude of 110° (rotation angle: 20°), (d) streamer at a longitude of 120° (rotation angle: 30°).

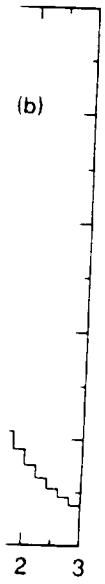

the total Lα
as a function
towards) the
cts the plane
streamer axis
ments to the
(b) streamer
angle: 20°),

to the need for (a) a different choice of boundary conditions in open regions than inside the streamer, (b) an extension of the model to different β values, and (c) the development of a 3-D model. We are presently working on these issues and expect to get a realistic simulation of open field regions shortly. Our goal is to attain a reasonable global model that simulates both streamers and coronal holes by achieving agreement between model predictions and existing observations. This is a method to fully determine the 3-D structure of streamers to within the resolution of the model and observations.

Traditionally, three-dimensional mapping of the electron density in coronal structures has been performed via the image reconstruction technique originally developed for X-ray tomography (Altschuler and Perry, 1972; Perry and Altschuler, 1973; Wilson, 1977), or via the already mentioned Van de Hulst's (1950) method. Both procedures have been subject to criticisms (Bagenal and Gibson, 1991) because of their heavy computational requirements. While the ideal method for a 3-D mapping has yet to be found, an alternative approach to devise theoretical models with free parameters that are calibrated against observational data, is being developed (Bagenal and Gibson, 1991). The present work uses this alternative approach and the results achieved so far indicate that it is worth pursuing. We conclude by pointing out that an agreement between model predictions and observations will allow us to determine the magnetic field vector throughout the streamer, thus providing a complete picture of these so far elusive structures.

Acknowledgements

The work of G. Noci and G. Poletto has been partially supported by ASI (Italian Space Agency). S. T. Suess acknowledges support from GNA (Gruppo Nazionale di Astronomia) and MURST (Ministero dell'Università e della Ricerca Scientifica) during his visit to Florence, where this work was initiated. Partial support by a grant from the Cosmic and Heliospheric Physics Branch of NASA is also acknowledged. A.-H. Wang and S. T. Wu are supported by NASA Grant NAGW-9.

References

Altschuler, M. D. and Perry, R. M.: 1972, *Solar Phys.* **23**, 410.
Bagenal, F. and Gibson, S.: 1991, *J. Geophys. Res.* **96**, 17663.
Beckers, J. M. and Chipman, E.: 1974, *Solar Phys.* **34**, 151.
Billings, D. E.: 1966, *A Guide to the Solar Corona*, Academic, San Diego, Ca.
Dollfus, A., Fort, B., and Morel, C.: 1968, *C. R. Acad. Sci. Paris* **266**, 1537.
Dollfus, A., Laffineur, M., and Mouradian, Z.: 1974, *Solar Phys.* **37**, 367.
Feldman, W. C., Asbridge, J. R., Bame, S. J., Fenimore, E. E., and Gosling, J. T.: 1981, *J. Geophys. Res.* **86**, 5408.
Foukal, P. V.: 1990, *Solar Astrophysics*, J. Wiley and Sons, New York, p. 12.
Gabriel, A. H.: 1971, *Solar Phys.* **21**, 392.
Gopalswamy, N., Kundu, M., and Szabo, A.: 1987, *Solar Phys.* **108**, 333.
Gosling, J. T., Borrini, G., Asbridge, J. R., Bame, S. J., Feldman, W. C., and Hansen, R. T.: 1981, *J. Geophys. Res.* **86**, 5438.

Hildner, E., Gosling, J. T., McQueen, R. M., Munro, R. H., Poland, A. J., and Ross, C. L.: 1975, *Solar Phys.* **42**, 163.
Illing, R. M. E. and Hundhausen, A. J.: 1986, *J. Geophys. Res.* **91**, 10951.
Kahler, S.: 1991, *Astrophys. J.* **378**, 398.
Kohl, J. L., Weiser, H., Withbroe, G. L., Noyes, R. W., Parkinson, W. H., Reeves, E. M., Munro, R. H., and MacQueen, R. M.: 1980, *Astrophys. J.* **241**, L117.
Kohl, J. L., Withbroe, G. L., Zapata, C. A., and Noci, G.: 1983, in M. Neugebauer (ed.), *Proc. of Solar Wind 5*, NASA Conf. Publ., CP 2280, p. 47.
Kopp, R. A. and Holzer, T. E.: 1976, *Solar Phys.* **49**, 43.
Koutchmy, S. L.: 1988, in R. C. Altrock (ed.), *Solar and Stellar Coronal Structure and Dynamics*, NSO Publ., p. 208.
Liebenberg, D. H., Bessey, R. J., and Watson, B.: 1975, *Solar Phys.* **40**, 387.
Newkirk, G. and Bohlin, J. D.: 1965, *Ann. Astrophys.* **28**, 234.
Noci, G., Kohl, J. L., and Withbroe, G. L.: 1987, *Astrophys. J.* **315**, 7036.
Perry, R. M. and Altschuler, M. D.: 1973, *Solar Phys.* **28**, 435.
Poland, A. I.: 1978, *Solar Phys.* **57**, 141.
Steinolfson, R. S., Suess, S. T., and Wu, S. T.: 1982, *Astrophys. J.* **255**, 730.
Suess, S. T., Richter, A. K., Winge, C. R., Jr., and Nerney, S.: 1977, *Astrophys. J.* **217**, 296.
Van de Hulst, H. C.: 1950, *Bull. Astron. Inst. Neth.* **11**, 135.
Wang, A.-H., Wu, S. T., Suess, S. T., and Poletto, G.: 1992, in E. Marsch, K. Sauer, and R. Schwenn (eds.), 'Solar Wind Seven', *COSPAR Colloq. 3*, Pergamon Press, Oxford, p. 311.
Wang, A.-H., Wu, S. T., Suess, S. T., and Poletto, G.: 1993, *Solar Phys.* **147**, 55 (this issue).
Wilson, D. C.: 1977, 'The Three-Dimensional Solar Corona: a Coronal Streamer', Ph.D. Thesis, University Colorado, Boulder.
Withbroe, G. L., Kohl, J. L., Weiser, H., Noci, G., and Munro, R. H.: 1982, *Astrophys. J.* **254**, 361.

A TWO-DIMENSIONAL MHD GLOBAL CORONAL MODEL: STEADY-STATE STREAMERS

A.-H. WANG, S. T. WU
Center for Space Plasma and Aeronomic Research and Department of Mechanical Engineering, The University of Alabama in Huntsville, Huntsville, AL 35899, U.S.A.

S. T. SUESS
Space Science Lab, ES52, NASA Marshall Space Flight Center, Huntsville, AL 35812, U.S.A.

and

G. POLETTO
Osservatorio Astrofisico di Arcetri, 50125 Firenze, Italy

(Received 4 August, 1992; in revised form 22 February, 1993)

Abstract. We describe a two-dimensional time-dependent, numerical, magnetohydrodynamic model for the determination of the physical properties of coronal streamers from the top of the transition zone ($R_\odot = 1$) to 15 $R_\odot$. Four examples are given: for dipole, quadrupole, and hexapole initial field topologies. The computed parameters are density, temperature, velocity, and magnetic field. In addition to the properties of the solutions, their accuracy is discussed. We use the model as the basis for a general discussion of the way boundary conditions are specified in this and similar simulations.

1. Introduction

We present results from a recently-developed numerical model of coronal structure. The immediate reasons for a new model were to extend the outer boundary farther from the Sun and to gain the experience necessary for development of a three-dimensional model. A result of this process has been a close examination of the physical details of the solution and how they depend on the way the boundary conditions are specified. An immediate application will be the simulation of streamers in support of the Ultraviolet Coronagraph and Spectroheliograph (UVCS) and the Large Angle Spectrometric Coronagraph (LASCO) on the Solar Heliospheric Observatory (SOHO). These instruments will be able to measure the temperature, density, and flow vector in the corona. With model calculations, it will be possible, for example, to estimate the magnetic field vector.

Numerical models of coronal structure have been published sporadically, at long intervals, over the past twenty years. The first (Pneuman and Kopp, 1971) demonstrated the feasibility of such models, treating isothermal flow and arriving at the solution by iterating on the electrical currents. However, a more efficient and flexible method is to consider an initial-boundary value problem in which the steady state is found holding the boundary conditions constant and allowing the solution to relax in time from an essentially arbitrary initial state. Steinolfson, Suess, and Wu (1982) applied this later technique to the analysis of a polytropic dipole configuration for a range of plasma β (ratio of internal pressure to mag-

Solar Physics **147**: 55–71, 1993.

netic pressure). Steinolfson (1989, 1991) and Guo *et al.* (1992) have used this steady-state solution as the basis for studying coronal mass ejections and streamer evolution with shear, which can be simulated using a nearly identical numerical model. Details of the numerical schemes and results can be found in the referenced publications.

We revisited this problem for the reasons mentioned above. However, we also consider that such complex numerical models are rarely without problems or uncertainties. When the models are used for analysis of data and for predictions, the only reliable validation is to develop an independent model and compare the results. Even when both (or all) models are fundamentally correct, this process generally leads to new or deeper understanding of the problem. In the present case, this is precisely what has happened. We have gained a better insight into the physical basis of the criteria which should be adopted in specifying boundary conditions. The results from this constitute an important part of the present study.

The physical and numerical simulation is described in Section 2. Section 3 details numerical models of dipole, quadrupole, and hexapole magnetic fields. Section 4 is a discussion of numerical precision of the solution and the boundary conditions, putting the discussion into context with earlier models so far as is possible. Section 5 contains our summary and conclusions.

2. The Physical and Numerical Simulation

We assume axisymmetric, single fluid, polytropic, time-dependent ideal magnetohydrodynamic flow and perform the calculation in a meridional plane defined by the rotational symmetry axis of the magnetic field. The coordinates are (r, θ, ϕ) with ϕ being the ignorable coordinate. For the magnetic field boundary condition, we take the radial field component at the lower boundary to be that given by a vacuum dipole, quadrupole, or hexapole potential magnetic field. The flow therefore has reflective symmetry across the equator and the calculation need be done in only one quadrant. The equations of motion that describe this flow are:

$$\frac{\partial \rho}{\partial t} + \frac{\partial}{\partial r}(\rho v_r) + \frac{\partial}{\partial \theta}\left(\rho \frac{v_\theta}{r}\right) = -\frac{2\rho v_r}{r} - \frac{\rho v_\theta}{r}\cot\theta\,, \tag{1a}$$

$$\frac{\partial v_r}{\partial t} + v_r \frac{\partial v_r}{\partial r} + \frac{B_\theta}{\mu\rho}\frac{\partial B_\theta}{\partial r} + \frac{1}{\rho}\frac{\partial p}{\partial r} - \frac{v_\theta}{r}\frac{\partial v_r}{\partial \theta} - \frac{B_\theta}{\mu\rho r}\frac{\partial B_r}{\partial \theta} = $$
$$= -\frac{GM_\odot}{r^2} + \frac{v_\theta^2}{r} - \frac{B_\theta^2}{\mu\rho r}\,, \tag{1b}$$

$$\frac{\partial v_\theta}{\partial t} + v_r \frac{\partial v_\theta}{\partial r} - \frac{B_r}{\mu\rho}\frac{\partial B_\theta}{\partial r} + \frac{v_\theta}{r}\frac{\partial v_\theta}{\partial \theta} + \frac{B_r}{\mu\rho r}\frac{\partial B_r}{\partial \theta} + \frac{1}{\rho r}\frac{\partial p}{\partial \theta} = $$
$$= \frac{B_r B_\theta}{\mu\rho r} - \frac{v_r v_\theta}{r}\,. \tag{1c}$$

$$\frac{\partial B_r}{\partial t} - \frac{\partial}{\partial \theta}\left(\frac{v_r B_\theta - v_\theta B_r}{r}\right) = \frac{1}{r}(v_r B_\theta - v_\theta B_r)\cot\theta \,. \tag{1d}$$

$$\frac{\partial B_\theta}{\partial t} + \frac{\partial}{\partial r}(v_r B_\theta - v_\theta B_r) = -\frac{1}{r}(v_r B_\theta - v_\theta B_r) \,. \tag{1e}$$

$$\frac{\partial p}{\partial t} + \gamma p \frac{\partial v_r}{\partial r} + v_r \frac{\partial p}{\partial r} + \frac{\gamma p}{r}\frac{\partial v_\theta}{\partial \theta} - \frac{v_\theta}{r}\frac{\partial p}{\partial \theta} = -\frac{\gamma p}{r}(2v_r + v_\theta \cot\theta) \,. \tag{1f}$$

The dependent variables are the density, ρ, the pressure, p, the radial and meridional velocities, v_r and v_θ, and the radial and meridional magnetic fields, B_r and B_θ. The constants $M_\odot$, G, γ, and μ are the solar mass, gravitational constant, the polytropic index and the magnetic permeability.

These equations are solved in a computational domain extending from the Sun ($1\ R_\odot$) to $15\ R_\odot$, from the pole to the equator. It is assumed that meridional flow is zero at the pole and equator. The grid is divided so that there are 37 gridpoints in the radial direction and 22 gridpoints in the meridional direction, with the radial grid size slowly increasing with radius. The meridional grid is divided so that points lie equidistant on either side of $\theta = 0$ and $\theta = 90°$, at $\theta = -2.25°$, $2.25°$, $6.75°$, ..., $87.75°$, $92.25°$. The algorithm adopted here is the Full-Implicit Continuous Eulerian (FICE) scheme described by Hu and Wu (1984). For time stepping a second-order accurate forward differencing scheme is used, with the step size being of the same order as given by the Courant condition because the magnetic field is calculated explicitly. Smoothing is used when gradients become too large, i.e., at shocks (which do not occur here). At the inner boundary, the flow is subsonic and sub-Alfvénic so that two of the six independent variables are calculated using compatibility relations (Hu and Wu, 1984). A brief summary of the compatibility conditions for the present model is given in the Appendix, along with details on how the boundary values and conditions are applied. We choose to specify the radial and meridional magnetic fields, temperature, and density. The radial and meridional flow speeds are computed from compatibility relations (i.e., Equations (A.1) and (A.2)). At the outer boundary, the flow is restricted to being both supersonic and super-Alfvénic. In this case, all variables at that boundary can be calculated by simple linear extrapolation from the first (or first two) grid points inside the boundary. In this study, we did not perform the comparison between the present boundary conditions and conventional boundary conditions. However, in a recent study by Sun (1991), it was shown that the statement of the boundary conditions in the Appendix eliminates the spurious waves generated by boundary disturbances and which can cause numerical instability.

We start with an essentially arbitrary initial state and allow the flow to relax in time while holding the boundary values constant. In the present case the initial flow field is a polytropic, hydrodynamic solution to the steady-state radial flow equation of motion (e.g., Parker, 1963) superimposed on a potential magnetic field. That this is neither a self-consistent nor stable solution to the steady-state MHD equations is irrelevant since the flow is allowed to evolve in time under the control

of the equations of motion. The main concerns are that the numerical solution be stable and of sufficient accuracy to define the physically interesting aspects of the solution, and that the relaxation proceed long enough that an acceptably close approximation to the steady state has been reached. We address these issues briefly in Section 4.

3. Detailed Results from Four Specific Models

We report here on four specific models. The results are grouped first according to the way in which the physical variables are plotted (i.e., either versus radius or versus polar angle) and second according to which of the four examples the plot is for. In these four examples, three magnetic field geometries are used: a dipole, a quadrupole, and a hexapole; the scalar potentials are therefore proportional to $P_2(\cos\theta)$, $P_3(\cos\theta)$, and $P_4(\cos\theta)$, respectively, where $P_n(\cos\theta)$ is the Legendre polynomial of degree n. There are two dimensionless free parameters: the polytropic index, γ, and the plasma β. We use $\gamma = 1.05$ in all cases, $\beta = 1.0$ for all three field geometries, and, in addition, do a dipole calculation for $\beta = 0.2$. In these case, β is evaluated at 1.0 $R_\odot$ at the equator, where the field strength is 1.67 G both for $\beta = 1.0$ and $\beta = 0.2$. For the high β cases, the base temperature and density are 1.8×10^6 K and 2.25×10^8 cm^{-3}. For the low β case, they are 1.44×10^6 K and 5.61×10^7 cm^{-3}. The three magnetic field geometries naturally lead to a single equatorial streamer, a mid-latitude streamer, and both an equatorial and a mid-latitude streamer for the dipole, quadrupole and hexapole, respectively.

Results from the four examples will be referred to as follows:

(a) Dipole, $\beta = 1.0$.
(b) Quadrupole, $\beta = 1.0$.
(c) Hexapole, $\beta = 1.0$.
(d) Dipole, $\beta = 0.2$.

The initial state temperature, density, and velocity profiles are shown in Figure 1. The temperature curves appear irregular due to the small change in temperature over the relatively large radial range – a consequence of the polytropic index being near unity. Only three significant figures were retained after the calculation so what is seen here is roundoff error in the plotted results rather than in the computed results.

The final, steady-state magnetic field geometries for the four cases are shown in Figure 2. Here is seen the well-known property that the flow is nearly radial beyond 3–4 $R_\odot$. The flow is field-aligned everywhere and field lines which cross the outer boundary reach to ∞. The streamers are those volumes which are magnetically closed (i.e., the field lines return to the surface of the Sun) and it is evident that relatively small volumes in the streamers remain magnetically closed in comparison to the initial state where all field lines were closed. These closed volumes are surrounded by a low density shell but, as will be shown below, the densities in the large coronal hole-like open regions are otherwise only slightly lower than in the

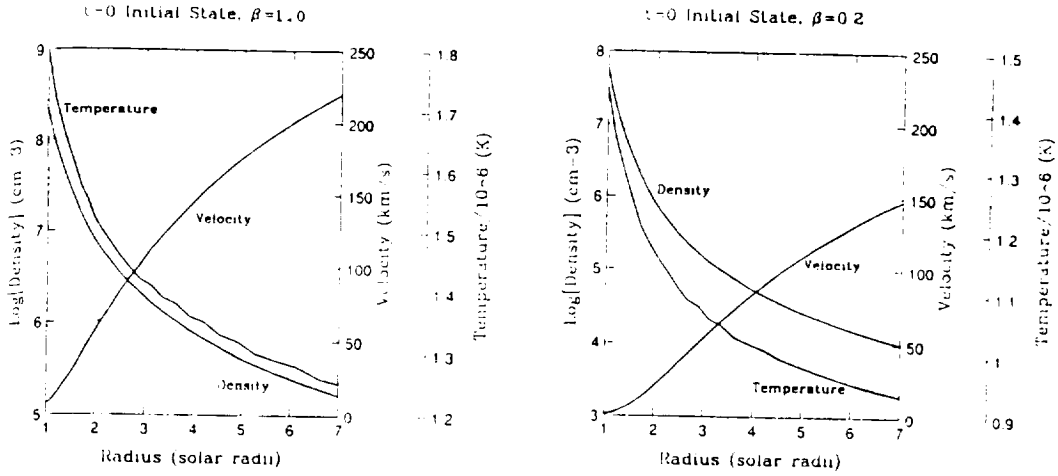

Fig. 1. Density, temperature, and velocity profiles in radius that were used for the initial ($t = 0$) state in the relaxation. On the left are the profiles for the $\beta = 1.0$ cases and on the right are the profiles for the $\beta = 0.2$ case. Note that, except for the velocity scales, the scales differ between the two panels. Because the polytropic index is near unity, temperature changes slowly with radius and the irregularities in the temperature profiles should be interpreted as noise.

streamers. In each panel of Figure 2, four dashed lines are shown and labelled A, B, C, or D. These lines indicate the radial directions used below to plot variables versus radius.

The physical times allowed for the relaxation in these four examples were: (a) 22.22 hours for the $\beta = 1.0$ dipole; (b) 16.67 hours for the $\beta = 1.0$ quadrupole; (c) 18.06 hours for the $\beta = 1.0$ hexapole; (d) 19.44 hours for the $\beta = 0.2$ dipole. These times are determined by how long it takes for any fluctuation to be advected out through the outer boundary of the solution domain. This in turn depends on how large the flow speed is and whether the fluctuations represent inward propagating waves. In general, the times listed above are the minimum required for a stationary fluctuation (i.e., non-propagating in the solar wind frame) to be advected from 1 $R_\odot$ to 15 $R_\odot$ at a typical flow speed in the open regions. This sometimes leads to small residuals in the relaxation near the outer boundary at 15 $R_\odot$, but the solutions inside 7 $R_\odot$ that are shown here are quite steady. This is another point that will be reviewed in Section 4.

Figures 3 and 4 are plots of density and radial velocity versus radius. The plots are made in the directions indicated in Figure 2 so that, for example, in each panel of Figure 3 the density is plotted in the four directions A, B, C, and D indicated in the corresponding panel of Figure 2. In both of Figures 3 and 4, the four panels corresponding to the four panels in Figure 2 are clearly labeled. The density profiles have been divided by their corresponding initial state ($t = 0$) profiles from Figure 1 because the density changes by several orders of magnitude between the Sun and 15 $R_\odot$. The plots here extend only to 7 $R_\odot$ because there is no new information

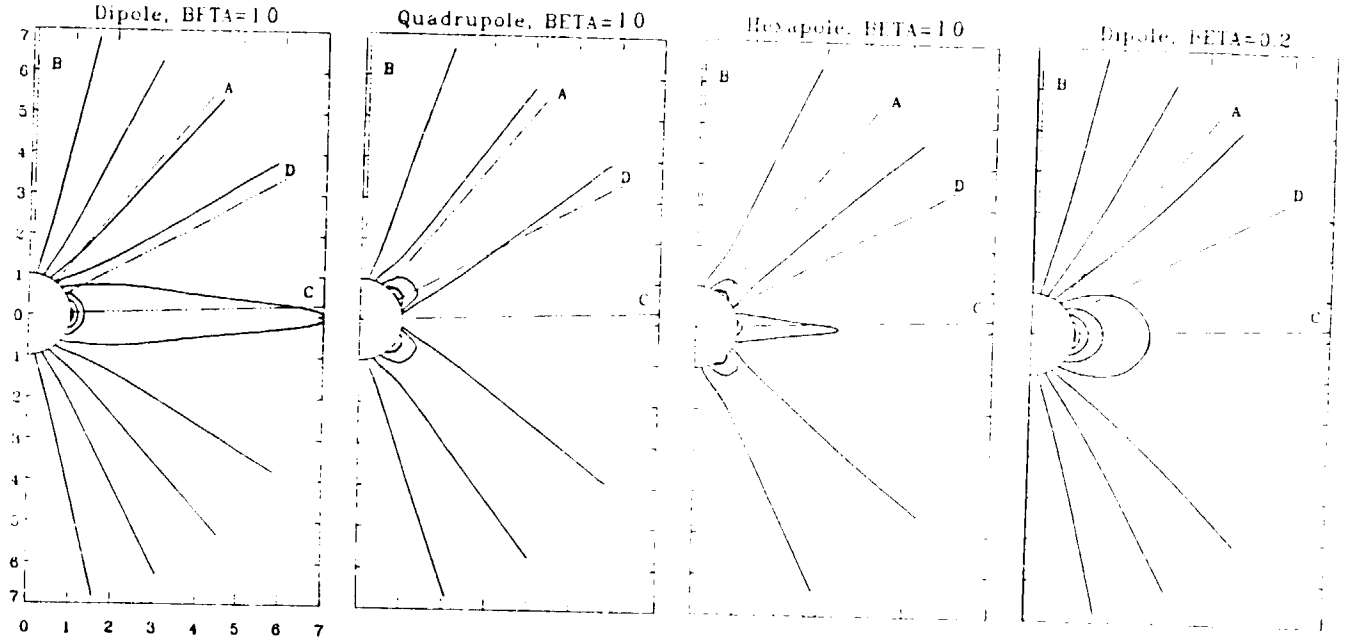

Fig. 2. Steady-state magnetic field-line plots for the four cases: (a) dipole, $\beta = 1.0$, (b) quadrupole, $\beta = 1.0$, (c) hexapole, $\beta = 1.0$, and (d) dipole, $\beta = 0.2$. The relaxation times allowed to reach these equilibria are: (a) 22.22 hours, (b) 16.67 hours, (c) 18.06 hours, (d) 19.44 hours, respectively. In each plot, four dashed lines are labelled 'A, B, C, or D'. These show the radial directions used for plotting the variables versus radius in each case. Thus, the $\beta = 1.0$ quadrupole plots will have variables plotted versus radius at the pole (B), at the edge of the polar open region (A), through the mid-latitude streamer (D), and in the equatorial open region (C). The dashed lines are along the directions of the grid. Since there is no grid point either exactly on the equator or exactly at the pole, these lines are slightly offset from those positions.

contain
Tu
enhan
concer
of 25
to that
profile
curves
the β
that is

Fig. 3.
labelled
for the
of Figu
Figure
density
50% ab

Relative Density

Relative Density

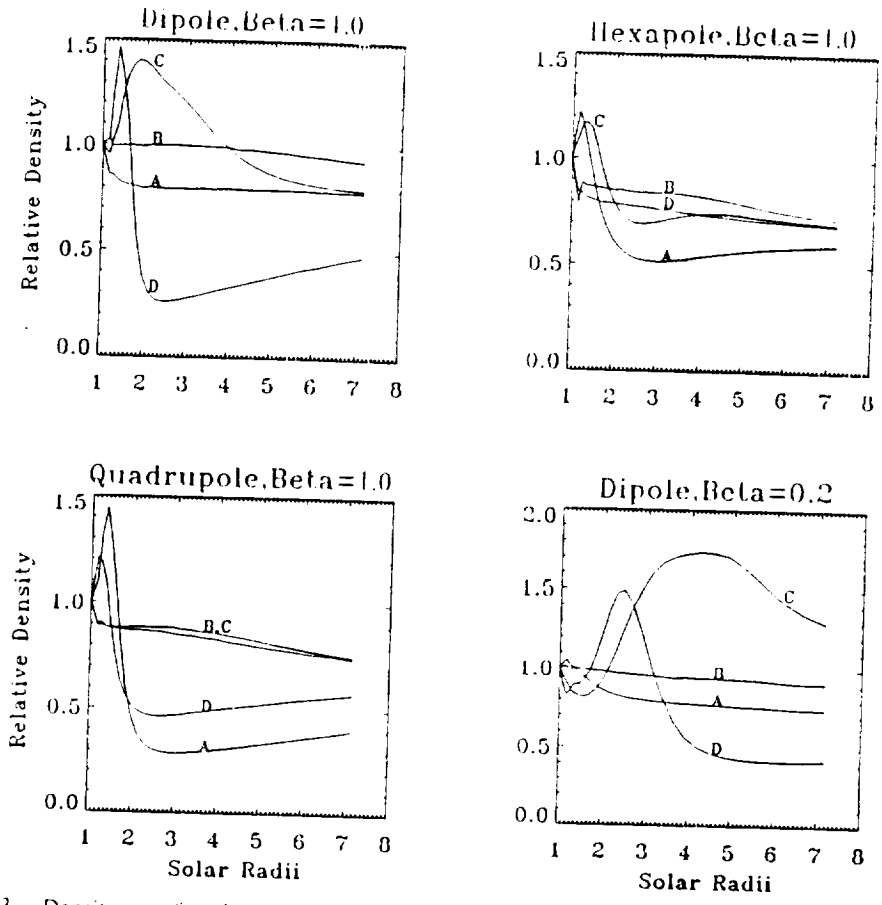

Fig. 3. Density as a function of radius. Each panel is for the corresponding case in Figure 2, as labelled. The curves are plotted along the directions shown in Figure 2. For example, the four curves for the $\beta = 1.0$ hexapole labelled A, B, C, D, are along the four directions shown in the third panel of Figure 2 and labelled in the same manner. Each curve has been divided by the initial profile (see Figure 1). A density enhancement is indicated by values greater than unity, and *vice versa*. The density concentrations in the streamers are clearly visible, generally being on the order of 25% to 50% above the initial state.

the $\beta = 1.0$ quadrupole plots will have variables plotted versus radius at the pole (B), at the edge of the polar open region (A), through the mid-latitude streamer (D), and in the equatorial open region (C). The dashed lines are along the directions of the grid. Since there is no grid point either exactly on the equator or exactly at the pole, these lines are slightly offset from those positions.

contained outside this radius – the flow is already supersonic and essentially radial.

Turning briefly to each figure individually, we begin by noting that a density enhancement is indicated by values greater than unity, and *vice versa*. The density concentrations in the streamers here are clearly visible, generally being on the order of 25% to 50% above the initial state. The base density for the $\beta = 1.0$ cases is close to that reported by Allen (1955) for the base of the quiet corona and the density profile shown here has generally the right behavior for streamers – as shown by curves C for cases (a), (c), and (d), and curve D in case (b). Curve D for case (a), the $\beta = 1.0$ dipole, is an example of the density deficit on the flank of a streamer that is typical of the results for all the examples. In contrast, the density in the

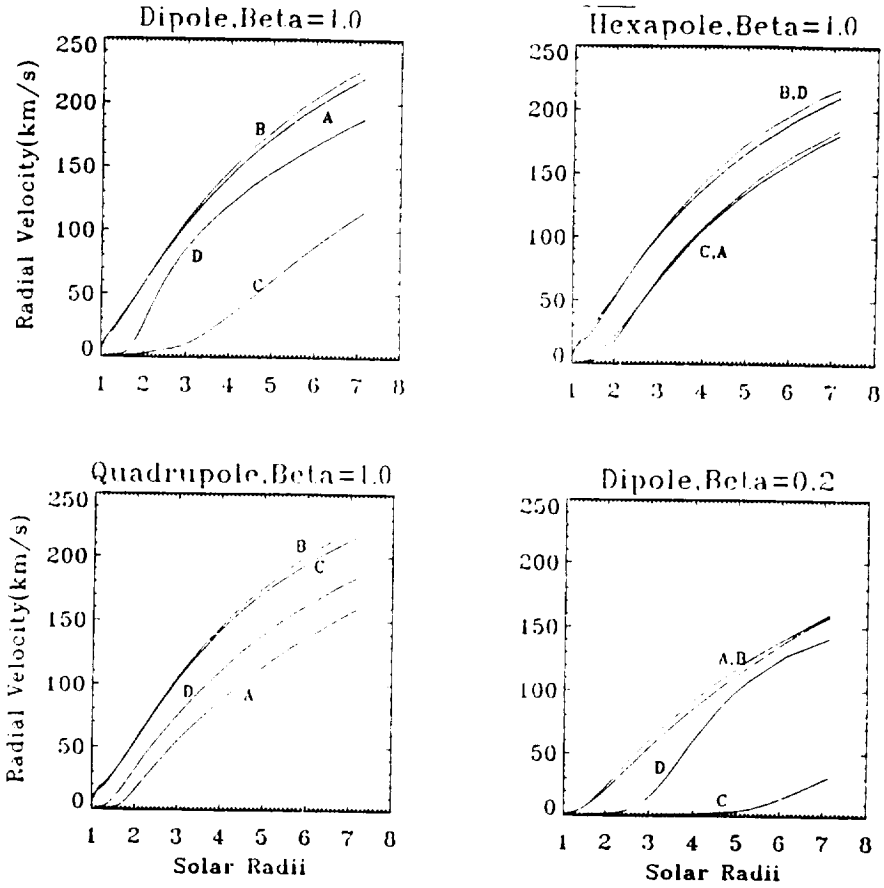

Fig. 4. Radial velocity as a function of radius. Each panel is for the corresponding case in Figure 2. The curves are plotted along the directions shown in Figure 2, as in Figure 3. The velocity inside the streamers is seen to be essentially zero.

centers of the open regions (curve B in all cases, curve C in case (b), and curve D in case (c)) is little different from the initial state, being only slightly smaller. This is only surprising when comparison is made to coronal hole observations (Munro and Jackson, 1977) wherein the density was reported to be more than an order of magnitude less than in streamers. This difference is a natural consequence of the properties of a polytropic model and the choice we have made for the boundary conditions on temperature and density – that they be independent of polar angle. The choice leads to both the high density shown here and the low flow speeds shown below on open field lines, irrespective of the open streamline geometry. To model true coronal hole flow with a polytropic gas would require at least an elevated temperature in the open regions and probably also a lower density at the base (Suess *et al.*, 1977; Suess, 1979).

The radial velocity is shown in Figure 4, at the positions indicated in Figure 2.

=1.0

7 8

0.2

7 8

se in Figure 2.
city inside the

nd curve D
naller. This
ions (Munro
an order of
uence of the
ie boundary
polar angle.
low speeds
geometry.
at least an
nsity at the

in Figure 2.

As described above, and as is generally the case in polytropic models, the flow speed in the open regions is similar to the undisturbed initial flow speed shown in Figure 1. In the streamer, the flow speed is essentially zero and it is reduced on the adjacent open field lines due, apparently, to the strongly inclined flow direction more than to geometry. The nonzero outflow above streamers (e.g., at $R = 7.14\ R_\odot$, at the equator of the $\beta = 1.0$ dipole) refers to the open field region above the streamer's cusp. The $\beta = 0.2$ dipole is the most extreme example of this – and the flow speed is nearly identical to the initial speed everywhere except on closed field lines, directly above the center of the streamer, and on the highly inclined field lines immediately adjacent to the streamer – where the difference is still rather small.

We do not plot the temperature since, due to the polytropic index being 1.05, it varies by only a few percent throughout the computation domain. However, this is an 'effective temperature' because a polytropic energy equation with a polytropic index of 1.05 is equivalent to a large amount of energy being added to the flow. Nowhere is the form of this energy specified, nor what the conversion and dissipation mechanisms are. However, it has been shown that a polytropic index on the order 1.05 is required to reproduce observations of coronal densities (Suess *et al.*, 1977).

Finally, the magnetically open regions, although euqivalent to coronal hole flows, do not simulate coronal holes because the flow speeds are far too small. To obtain reasonable flow speeds in this model it would be necessary to have the temperature vary across the base of the open region – which is well within the capability of the model. Such a variation has been shown to reproduce all the known properties of coronal hole flow and lead to accurate simulations of the geometry, with the effective temperature being larger in the center of the hole than at the edge (Suess *et al.*, 1977). In contrast to the open regions, the densities in the closed regions are similar to observed streamer densities and we feel this model is therefore a good approximation to streamer geometry. The temperature must still be qualified as an effective temperature, but can be used for diagnostic purposes in combination with planned observations on SOHO/UVCS.

Some of the results can be better viewed and more easily understood when plotted versus polar angle at different heliocentric distances, than versus radius at constant polar angles. Such plots are shown for the density, radial velocity, and total field strength in Figures 5, 6, and 7, respectively.

Figure 5 shows the density drop adjacent to the streamer. In the panel for the $\beta = 1.0$ dipole, this drop is quite large, well resolved, and leads into the density enhancement inside the equatorial streamer. The only place this does not occur is at the base – where the density is held constant. The width of the density enhancement in the streamer decreases with height, just as the width of the streamer itself decreases with height (e.g., Figure 2). Essentially the same thing is seen for the $\beta = 0.2$ dipole wiht the following quantitative differences: (i) The streamer is much higher and wider. (ii) The density depletion on the flanks has a smaller amplitude.

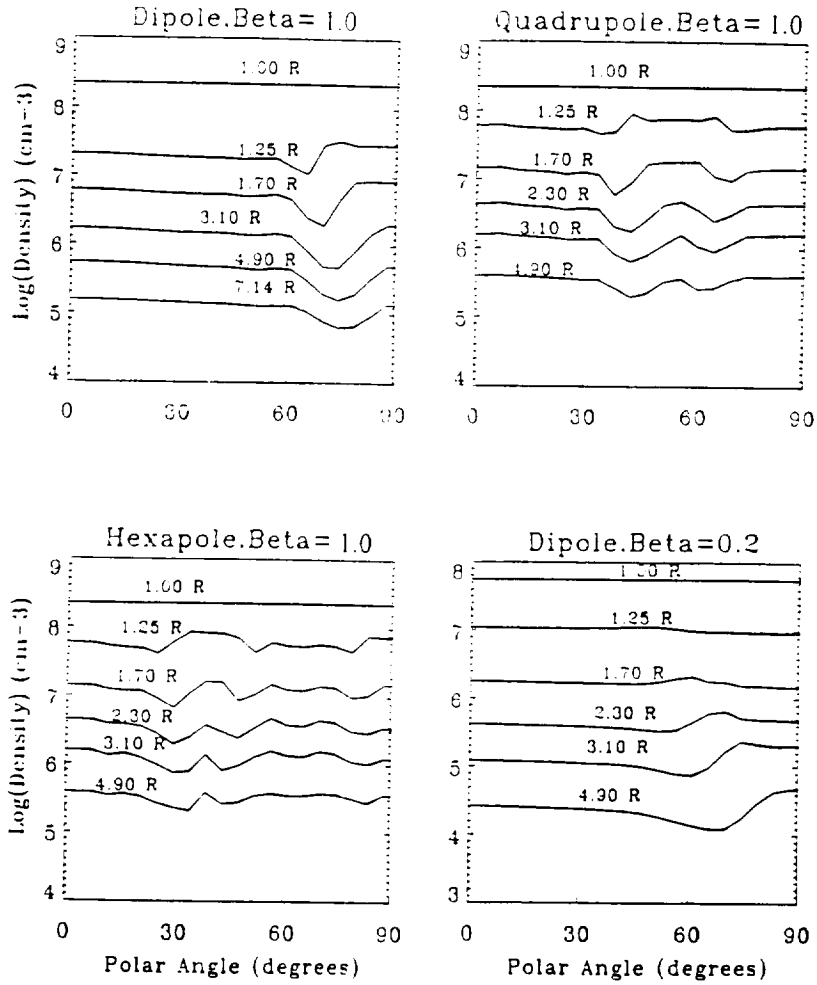

Fig. 5. Density versus polar angle, between the pole (0°) and the equator (90°). Each of the curves is labelled according to the heliocentric distance it refers to. Thus, the curves labelled 1.70 R indicate the density at 1.70 $R_\odot$ heliocentric radius. The density at the base is constant and so the curves there are flat. Above the base, there is a small density enhancement in the streamer (ca. 5% to 50%) and a trough in density at the edge of the streamer. In the middle of the open region, the density is very close to what it was in the initial state (see also Figure 3). The reason it is not small is that we have used constant temperature and density at the base. To produce a true coronal hole-like profile would have required at least an increase in the temperature at the base of the open region (Suess *et al.*, 1977).

These differences are the primary reason we conclude that solar streamers are better described by a $\beta = 1.0$ plasma than by a $\beta = 0.2$ plasma. Qualitatively, a similar result is found for the quadrupole and hexapole. However, it is obvious that the hexapole is only marginally resolved with the present grid density – there is really only one meridional grid point inside the mid-latitude streamer at any given height.

The radial velocity in Figure 6 drops precipitously from the magnetically open region to the inside of the streamer. That the velocity is not identically zero inside the streamer is a result of numerical diffusion and is a measure of this numerical artifact in the FICE scheme. For example, at 1.70 $R_\odot$ in the $\beta = 1.0$ dipole, the velocity drops from ca. 60 km s^{-1} at the edge of the streamer to about 3 km s^{-1} inside the streamer. 3 km s^{-1} is hardly above the noise level in the plots and the associated kinetic energy is too small to affect the dynamics of the solution. Such 'slippage' will, nevertheless, occur in all numerical solutions. At larger heights (e.g., 4.90 and 7.14 $R_\odot$) there is small, but finite flow near and in the neutral sheet dividing regions of opposite magnetic polarity. This is qualitatively like what is observed in the solar wind in the interplanetary medium. The $\beta = 0.2$ dipole again exhibits properties unlike the Sun in the sense that the very low flow speeds inside the streamer seem to still exist even at 7.14 $R_\odot$ – far outside the observed extent of closed streamers.

Figure 7 shows the variation of the total magnetic field strength, $(B_r^2 + B_\theta^2)^{1/2}$, across the streamers. The most interesting thing to note in these plots is the enhancement in total field strength on the flanks of the streamers. This is what 'confines' the streamers. The field strength for the $\beta = 0.2$ dipole is seen to vary smoothly, with little distinct evidence of the streamer. This is just another indication that the presence of the plasma has had little effect on the field geometry in this low-β case.

4. Accuracy and Stability of Calculations

This numerical model has been found to be weakly subject to the Courant condition on size of time step. Therefore, the size of the time step decreases as the largest values of the temperature and magnetic field increase – along with the maximum sound and Alfvén speeds anywhere in the grid. Counteracting this, the higher characteristic speeds lead to a somewhat faster relaxation time. However, generally shorter time steps are required for smaller β calculations. The flow speed also plays an important role in determining the relaxation time to a steady state – the initial state is a disequilibrium configuration. This imbalance must have time to be advected from the base through the outer boundary. The physical time this takes can be estimated by taking a typical (but small) value for the flow speed and caculating how long it would take the plasma to flow at this speed from the base to the outer boundary. For example, at 150 km s^{-1}, to 15 $R_\odot$, this takes 18 hours (relaxation times we have used here are given in Figure 1).

A second consideration is gridpoint resolution. The grid used in these examples is 4.5° in latitude and about 0.24 $R_\odot$ in radius near the base – increasing slowly with radius. This is sufficient to adequately resolve the geometry and flow on the scale shown in Figure 2. However, if finer scale information is required in, for example, the core of the streamers, a denser grid would be required.

Always a serious consideration in these time-dependent, non-Cartesian MHD calculations is the conservation of magnetic flux – that $\nabla \cdot \mathbf{B} = 0$ is maintained

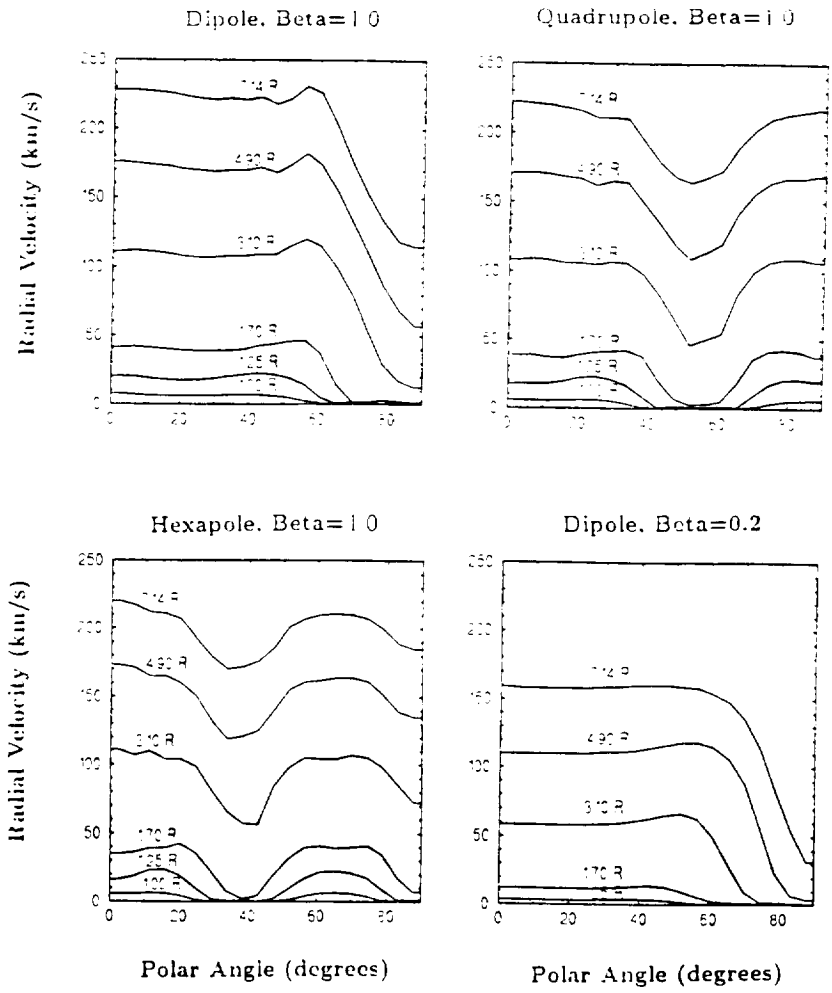

Fig. 6. Radial velocity versus polar angle, between the pole and the equator. Each curve, plotted for different heliocentric distance, is labelled in the same manner as in Figure 5. The velocity in the magnetically closed regions is essentially zero. The reason it is not identically zero is that there is a small amount of numerical diffusion – quite small as indicated by the velocity being less than 10 km s^{-1} inside the $\beta = 1.0$ dipole streamer at 2.30 $R_\odot$.

at all times. The condition is maintained here through accurate differencing rather than a self-correcting scheme. No anomalous acceleration due to errors in flux conservation is apparent in the results. The numerical scheme is pressure-based so it is limited by stability to large and moderate β values (e.g., $\beta \geq 0.1$) – which turns out to be the same restriction for maintaining $\nabla \cdot \mathbf{B} = 0$ to the required degree.

Finally, the energy equation

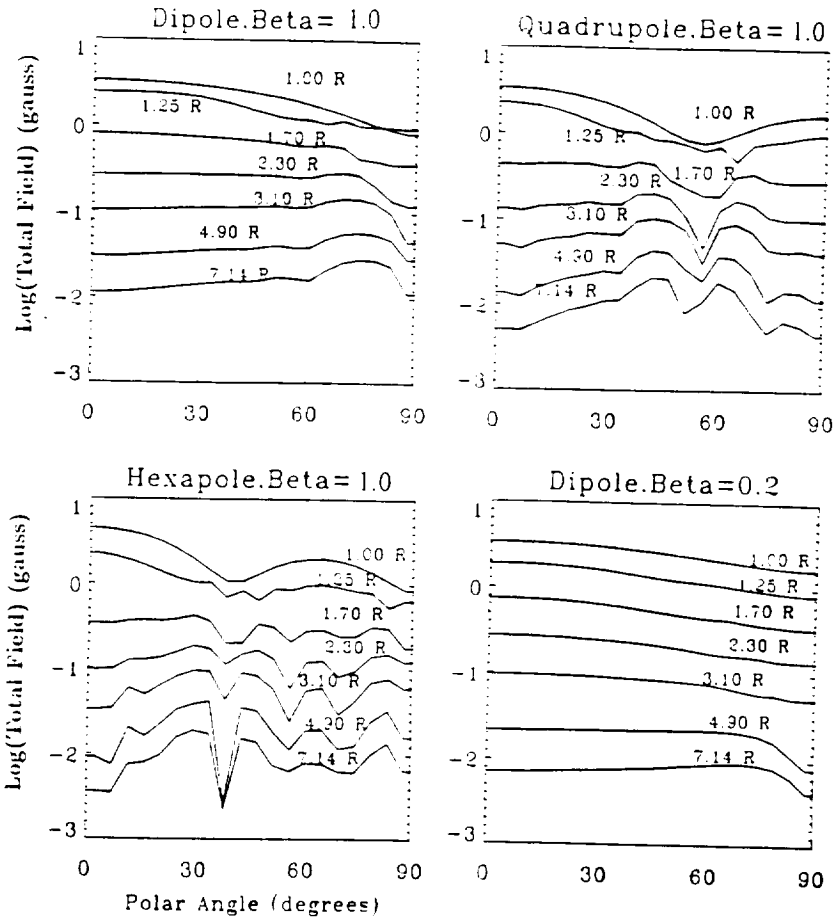

Fig. 7. The total magnetic field, $(B_r^2 + B_\theta^2)^{1/2}$, versus polar angle, between the pole and the equator. Each curve, plotted for different heliocentric distance, is labelled in the same manner as in Figure 5. The field in the vicinity of the current sheet above the cusp in the streamers has a greatly reduced amplitude, as would be expected. The effect is amplified above the mid-latitude streamers.

$$\left(\frac{\partial}{\partial t} + \mathbf{v}\cdot\nabla\right)\left(\frac{p}{\rho^\gamma}\right) = 0$$

reduces to $\mathbf{v}\cdot\nabla(p/\rho^\gamma) = 0$ when a steady state is reached, which means that (p/ρ^γ) is then a streamline constant. This becomes an analytic test of the achievement of a steady-state solution in our case. The boundary values of p and ρ are the same at all latitudes. Therefore, $(p/\rho^\gamma) = 0$ has the same value everywhere in the computation regime as it has on the boundary if a steady state has been reached. We have checked this for the cases shown in Figure 2 and find that for the dipole and quadrupole it is constant to within a maximum of 1% and for the hexapole it is constant to within a maximum of 4% (average values over the whole grid are less than 1% in all cases).

5. Discussion

The new feature of this model, with respect to analogous simulations, is the extension of the outer boundary to 15 $R_\odot$. This is not a conceptual advance, but this and the stability and ruggedness of the code make it very useful for simulating realistic coronal conditions. We present new results for quadrupole and hexapole fields, with their accompanying mid-latitude streamers and open magnetic field regions. The Alfvén speed ranged between 800 km s^{-1} and a few tens of km s^{-1}. This is lower than is believed appropriate for the corona (Suess, 1988), but we expect our model will now enable simulations with higher Alfvén speeds.

When comparing our results to those of Steinolfson, Suess, and Wu (1982; henceforth referred to as SSW), an interesting and important difference becomes apparent. In the present calculation, we have held the density and temperature constant at the base, allowing the velocity (and, hence, the mass flux) to 'float' with time in accordance with the compatbility relations determining the velocity from the solution inside the computational domain. In contrast, SSW hold the temperature and velocity constant at the base and allow the density to change according to the compatibility relationships. SSW determine the location of the streamer by locating closed field lines and allowing the velocity to decrease to zero at the feet of these field lines. A consequence is that inside the streamer, the final density is considerably higher than the initial density and this is the primary reason for the quantitative differences between their results and ours.

There is an important consequence of this difference in boundary conditions between SSW and the present calculation: the plasma β is computed using the temperature, density, and magnetic field at the equator and at 1 $R_\odot$. This is invariant in the present calculation, but in SSW this number is different in the final, steady state than at the beginning: there β was computed using the initial values. Therefore, in SSW in the steady-state solution is actually larger than stated for each example they did. Thus, our calculation for a dipole with $\beta = 0.2$ (case (d)) corresponds to cases for $\beta \leq 0.1$ in SSW. We feel that the way we have done the analysis more closely corresponds to what occurs and what is physically known for the Sun and therefore leads to a more precise definition of the problem. So, we conclude that the present study has demonstrated a preferable treatment of the boundary conditions in comparison to earlier calculations.

A consequence of the precise examples we have done in cases (a) through (d), with constant temperature and density, is the flow speed and high density in the magnetically open regions – in comparison to what is believed to be the case in solar coronal holes. This is a natural consequence of using a polytropic gas in which the flow speed is strongly dependent on base temperature. It also does not reflect suggestions from analysis of Skylab data that densities at the base of coronal holes may be a factor of two smaller than at the base of streamers (G. Noci, private communication). In a continuation of this study, we will produce models with varying temperature and density at the base. The variation in temperature

will, because it is an 'effective temperature', reflect a difference in energy balance and distribution between the base of coronal holes and streamers instead of a true temperature difference.

Acknowledgements

AHW and STW are supported by NASA Grant NAGW-9. STS has been supported by a grant from the Cosmic and Heliospheric Physics of NASA. GP acknowledges support from ASI (Italian Space Agency) and the University of Alabama in Huntsville.

Appendix. The Inner Boundary Conditions According to the Projected Normal Characteristic Method: a 2D Case

The inner boundary conditions are obtained according to the method of projected characteristics (Nakagawa, Hu, and Wu, 1987) with the FICE algorithm (Hu and Wu, 1984). For the two-dimensional case, the Alfvénic mode does not exist, therefore, there are six eigenvalues. These six eigenvalues lead to six projected normal characteristics and to six compatibility equations (see Wang, 1992; for derivation). At the inner boundary, since $v_r \geq 0$ and $v_r < V_s, V_f$, the characteristics $dr/dt = v_r - V_s$ and $dr/dt = v_r - V_f$ are towards the lower boundary from interior (i.e., outgoing) and need to be considered. There are four incoming characteristics (v_r, $v_r + V_s$, $v_r + V_f$, and one that is degenerate because of the model symmetries), so four variables can be specified at the boundary. Two other variables need to be calculated from related compatibility equations. We choose the values of B_r, B_θ, ρ, and T to be specified, leaving two quantities (i.e., v_r and v_θ) to be computed according to following compatibility equations:

$$\frac{\partial v_r}{\partial t} = \frac{V_s B_- + V_f C_-}{\rho V_s V_f (V_s^2 - V_f^2)}, \tag{A.1}$$

$$\frac{\partial v_\theta}{\partial t} = \frac{V_s (v_A^2 - V_s^2) B_- - V_f (V_f^2 - V_A^2) C_-}{V_s V_f (V_f^2 - V_s^2) B_r B_\theta}. \tag{A.2}$$

with the corresponding variables simplified in two dimensions as follows:

$$v_A^2 = b_r^2 = \frac{B_r^2}{\rho}, \tag{A.3}$$

$$a^2 = \gamma R T, \tag{A.4}$$

$$b^2 = \frac{(B_r^2 + B_\theta^2)}{\rho}, \tag{A.5}$$

$$V_f^2 = \frac{1}{2} a^2 + b^2 + [(a^2 + b^2)^2 - 4 a^2 b_r^2]^{1/2}. \tag{A.6}$$

$$V_s^2 = \frac{1}{2}a^2 + b^2 + [(a^2+b^2)^2 - 4a^2b_\theta^2]^{1/2}. \tag{A.7}$$

$$\begin{aligned}
B_- = {} & \rho(V_f^2 - V_A^2)V_f(v_r - V_f)\frac{\partial v_r}{\partial r} - B_r B_\theta V_f(v_r - V_f)\frac{\partial v_\theta}{\partial r} - \\
& -(V_f^2 - V_A^2)(v_r - V_f)\frac{\partial p}{\partial r} - B_\theta V_f^2(v_r - V_f)\frac{\partial B_\theta}{\partial r} + \\
& +\rho(V_f^2 - V_A^2)V_f V_\theta \frac{1}{r}\frac{\partial v_r}{\partial \theta} - \frac{B_\theta v_\theta V_f^2}{r}\frac{\partial B_\theta}{\partial \theta} - \\
& -[\rho a^2(V_f^2 - V_A^2) + B_\phi^2) + B_r B_\theta V_f v_\theta]\frac{1}{r}\frac{\partial v_\theta}{\partial \theta} - \\
& -\left[v_\theta(V_f^2 - V_A^2) + \frac{B_r B_\theta V_f}{\rho}\right]\frac{1}{r}\frac{\partial p}{\partial \theta} - \frac{B_\theta v_f^3}{r}\frac{\partial B_r}{\partial \theta} - \\
& -\frac{v_r V_f^2}{r}[2\rho(V_f^2 - V_A^2) - B_\theta^2] - \frac{V_f^2 B_\theta v_\theta}{r}(B_r + B_\theta \operatorname{ctg}\theta) - \\
& -\frac{v_\theta V_f^2}{r}[\rho(V_f^2 - V_A^2) - B_\theta^2]\operatorname{ctg}\theta - \frac{v_r v_\theta B_\theta B_r V_f}{r} - \\
& -\frac{\rho V_f V_\theta^2}{r}(V_f^2 - V_A^2) + \frac{V_f^3 B_\theta^2}{r} + \rho g(V_f^2 - V_A^2)V_f .
\end{aligned} \tag{A.8}$$

$$\begin{aligned}
C_- = {} & \rho(V_A^2 - V_s^2)V_s(v_r - V_s)\frac{\partial v_r}{\partial r} - B_r B_\theta V_f(v_r - V_s)\frac{\partial v_\theta}{\partial r} - \\
& -(V_A^2 - V_s^2)(v_r - V_s)\frac{\partial p}{\partial r} + B_\theta V_s^2(v_r - V_s)\frac{\partial B_\theta}{\partial r} + \\
& +\rho(V_A^2 - V_s^2)V_s V_\theta \frac{1}{r}\frac{\partial v_r}{\partial \theta} - \frac{B_\theta v_\theta V_s^2}{r}\frac{\partial B_\theta}{\partial \theta} - \\
& -[\rho a^2(V_A^2 - V_s^2) - B_\phi^2) + B_r B_\theta V_s v_\theta]\frac{1}{r}\frac{\partial v_\theta}{\partial \theta} - \\
& -\left[v_\theta(V_A^2 - V_s^2) + \frac{B_r B_\theta V_f}{\rho}\right]\frac{1}{r}\frac{\partial p}{\partial \theta} + \frac{B_\theta v_s^3}{r}\frac{\partial B_r}{\partial \theta} + \\
& +\frac{v_r V_s^2}{r}[2\rho(V_s^2 - V_A^2) + B_\theta^2] - \frac{V_s^2 B_\theta v_\theta}{r}(B_r + B_\theta \operatorname{ctg}\theta) + \\
& +\frac{v_\theta V_s^2}{r}[\rho(V_s^2 - V_A^2) - B_\theta^2]\operatorname{ctg}\theta + \frac{v_r v_\theta B_\theta B_r V_s}{r} - \\
& -\frac{\rho V_s V_\theta^2}{r}(V_A^2 - V_s^2) - \frac{V_s^3 B_\theta^2}{r} + \rho g(V_A^2 - V_s^2)V_s g .
\end{aligned} \tag{A.9}$$

Since the ideal MHD equations have been used, flow is parallel to the magnetic field lines. Thus we determine B_θ from the relation $B_r v_\theta = v_r B_\theta$.

A TV
Allen, C.
Guo, W. I
M. E.
Hu, Y. Q.
Munro, R.
Nakagawa
Parker, E.
Pneuman,
Steinolfso
54, 2(
Steinolfso
Steinolfso
Suess, S.
Suess, S.
Proce
Suess, S.
Sun, M. T
Wang, A.-

(A.7)

References

Allen, C. W.: 1955, *Astrophysical Quantities*, Cambridge University Press, London.

Guo, W. P., Wang, J. F., Liang, B. X., and Wu, S. T.: 1992, in Z. Švestka, B. V. Jackson, and M. E. Machado (eds.), 'Eruptive Solar Flares', *IAU Symp.* **133**, 381.

Hu, Y. Q. and Wu, S. T.: 1984, *J. Comput. Phys.* **55**(1), 33.

Munro, R. J. and Jackson, B. V.: 1977, *Astrophys. J.* **213**, 874.

Nakagawa, Y., Hu, Y. Q., and Wu, S. T.: 1987, *Astron. Astrophys.* **179**, 354.

Parker, E. N.: 1963, *Interplanetary Dynamical Processes*, Interscience, New York.

Pneuman, G. and Kopp, R. A.: 1971, *Solar Phys.* **18**, 258.

Steinolfson, R. S.: 1989, in J. H. Waite, Jr., J. L. Burch, and R. L. Moore (eds.), *Geophys. Monograph* **54**, 269, American Geophysical Union, Washington, D.C.

Steinolfson, R. S.: 1991, *Astrophys. J.* **382**, 677.

Steinolfson, R. S., Suess, S. T., and Wu, S. T.: 1982, *Astrophys. J.* **255**, 730.

Suess, S. T.: 1979, *Space Sci. Rev.* **23**, 159.

Suess, S. T.: 1988, in R. C. Altrock (ed.), *Solar and Stellar Coronal Structure and Dynamics, Proceedings of the 9th Sacramento Peak Summer Symp.*, Sunspot, New Mexico, p. 130.

Suess, S. T., Richter, A. K., Winge, C. R., Jr., and Nerney, S.: 1977, *Astrophys. J.* **217**, 296.

Sun, M. T.: 1991, Ph.Dissertation, University of Alabama in Huntsville.

Wang, A.-H.: 1992, Ph.Dissertation, University of Alabama in Huntsville.

(A.8)

(A.9)

netic